International Journal of Plasticity 155 (2022) 103306

Contents lists available at ScienceDirect

International Journal of Plasticity

journal homepage: www.elsevier.com/locate/ijplas

# Substructure-sensitive crystal plasticity with material-invariant parameters

Shahram Dindarlou, Gustavo M. Castelluccio *

*School of Aerospace, Transport and Manufacturing, Cranfield University, Cranfield, UK*

ARTICLE INFO

*Keywords:*
Dislocation substructures
Crystal plasticity
Mesoscale material-invariant parameterization
Single crystals

ABSTRACT

Even though crystal plasticity models have been available for decades, the quantification of material parameters is still a matter of debate. Polycrystalline experimental results can normally be reproduced by multiple sets of parameters, raising concerns about the best parameterization to predict the grain-level response. This work presents a novel physics-based crystal plasticity model based on mesoscale dislocation substructures, which are used to characterize material parameters independently. We employ a unique set of parameters with known uncertainty to reproduce the mechanical response of FCC single- and poly-crystals. We demonstrate that mesoscale parameters are material-invariant and can be used to model FCC metals with similar dislocation substructures such as for Cu, Ni and Al. Furthermore, the model is validated by comparing to experimental single- and poly-crystalline stress–strain curves and mesoscale dislocation substructure images. This novel modeling approach is intrinsically designed to predict the response of materials with similar dislocation substructures without the need of single crystal experimental data for calibration.

## 1. Introduction

Crystal plasticity constitutive models have been extensively used to represent the effects of crystallographic orientation on the mechanical response of metallic materials (Nguyen et al., 2021; Lu et al., 2019; Roters et al., 2010; Trusov and Shveykin, 2013). Myriads of phenomenological and physics-based formulations have quantified model parameters by fitting simulations to the macroscopic stress–strain response of polycrystals. This approach is sound to predict the homogenized response of polycrystals such as the roles of texture or the stochastic nature of cracking controlled by the microstructure. However, recent research efforts (El Shawish and Cizelj, 2017; Pirgazi and Kestens, 2021) have demonstrated that parameters cannot be uniquely identified and cannot capture in detail the local response at or below the grain scale.

In spite of being formulated to describe the crystalline response, crystal plasticity simulations are not often compared to single crystal experiments. One exception is the work by Arsenlis and Parks (2002), whose model reproduced the response of some Al single crystals only up to 10% strain. Similarly, Bertin and co-workers (Bertin et al., 2013) developed an advanced hybrid modeling approach that considered both glissile and stored dislocation densities. This model reproduced accurately the mechanical response of single crystal oriented for multiple slip but not for single slip. Moreover, neither approach compared models to polycrystal experiments or proposed a clear strategy to determine parameters.

More recently, Khan and coworkers (Khan et al., 2015) modeled the mechanical response of Al single crystals at different strain rates. Their work successfully predicted the crystal response up to 20% strain under quasistatic loading for two orientations with

* Corresponding author.
*E-mail address:* castellg@cranfield.ac.uk (G.M. Castelluccio).

https://doi.org/10.1016/j.ijplas.2022.103306
Received 7 December 2021; Received in revised form 6 April 2022
Available online 27 April 2022
0749-6419/© 2022 The Authors. Published by Elsevier Ltd. This is an open access article under the CC BY license (http://creativecommons.org/licenses/by/4.0/).

high Schmid factor and limited cross slip. However, the predictive power diminishes for higher strain rates, which highlights the difficulties in identifying parameters or model forms that work for various loading conditions. Moreover, their work also omits the comparison to polycrystal data and a parameter identification strategy.

El Shawish and Cizelj (2017) introduced an optimization scheme to identify crystal plasticity parameters through the simultaneous fitting of single- and poly-crystal experimental stress–strain of austenitic stainless steel. Their approach demonstrated that multiple sets of parameters can reproduce the experiments with similar accuracy as a result of shallow objective functions with multiple local minima. Furthermore, they showed that these parameters can yield different grain-level response, which highlights the need for physics-based rather than mathematics-based strategies for parameter identification.

A different physics-based approach was proposed by Chandra et al. (2018), who employed dislocation dynamic simulations to parameterize the thermal stress and the initial hardening in crystal plasticity. Their work successfully reproduced the mechanical response of various crystals using a set of parameters for each orientation, which were subsequently averaged to predict the polycrystalline response. Although this approach does not predict single- and poly-crystals responses with a single parameterization, it demonstrates that by predicting single crystals we can approximate the behavior of polycrystals; notably, the inverse is not true in general. In the context of cyclic plasticity, Castelluccio and McDowell (2017) also demonstrated that a crystal plasticity model capable of predicting single crystal responses has good predictive power over polycrystals. Their approach relied on the independent estimation of parameters characterized by the morphology of mesoscale dislocation substructures.

This work innovates with a substructure-sensitive crystal plasticity approach that predicts the monotonic response of single and poly-crystals, simultaneously. We rely on a physics-based strategy for the independent identification of parameters by assimilating changes in the mesoscale substructure to a phase transformation among stable configurations. We demonstrate that mesoscale parameters are intrinsic to the structures and the same values apply to different FCC metals such as Cu, Ni and Al at similar homologous temperatures. Hence, mesoscale parameters are material-invariant for metals with similar dislocation substructures. As a result, our crystal plasticity approach is intrinsically built to predict single- and poly-crystalline response across systems with similar dislocation substructures without the need for unique single crystal experimental data for calibration.

## 2. Substructure-sensitive crystal plasticity model

In the absence of grain boundaries and precipitates, strain hardening in metallic materials arises from the production of dislocation locks with different strengths (e.g., Lomer–Cottrell, Hirth). Hähner (1996) and Kuhlmann-Wilsdorf and Comins (1983) argued that screw and edge dislocations trapped in dislocation locks can evade by cross slip and climb, respectively. Since climb is less likely to occur in FCC metals at low homologous temperatures, edge segments remain sessile and form immobile athermal dislocation walls. On the other hand, screw segments evade from locks via cross slip to annihilate and make dislocation free regions. This formation mechanism relies on cross slip and results in thermally-activated wall structures: Profuse cross slip enables equiaxed dislocation structures and refined walls upon increasing temperature or strain. On the contrary, at low strain, low temperature, or high Schmid factor, cross slip is not favored, resulting in athermal and anisotropic wall structures.

Thermal and athermal dislocation structures coexist throughout the stress–strain curve. Upon loading, initial coplanar dislocations lead to elongated athermal structures that eventually transition into more equiaxed cells due to the activation of profuse cross slip. As a result, the mechanical response presents multiple hardening stages associated with different structures. Hansen et al. (2001, 2006) identified three types of structures (I, II and III) according to their orientations and related their hardening to their dominant dislocation substructure. A similar relation between hardening and structures was found by Sard and Weil (1970), who showed that low and high hardening rates relates to elongated and equiaxed cell structures, respectively. As shown by Castelluccio and McDowell (2017) for cyclic deformation, the partition of plastic deformation among slip system can serve as a predictor for the dominant substructure morphology. Next, we present a model that predicts the morphology of the dominant dislocation structure from the partition of plasticity across slip planes.

### 2.1. Crystal plasticity model

Following the foundations of crystal plasticity for large deformations (Rice, 1971; Peirce et al., 1983), the total deformation gradient, $F$, is characterized by the common elastic, $F^e$, and plastic, $F^p$, multiplicative decomposition, i.e.,

$$F = F^e \cdot F^p. \tag{1}$$

The time derivative of the plastic deformation gradient, $\dot{F}^p$, relates to the isoclinic intermediate configuration plastic velocity gradient, $L^p$, such that

$$\dot{F}^p = L^p \cdot F^p = \sum_{\alpha=1}^{N_{sys}} \dot{\gamma}^\alpha (s^\alpha \otimes m^\alpha) \cdot F^p, \tag{2}$$

where $\dot{\gamma}^\alpha$ is the shear rate while $s^\alpha$ and $m^\alpha$ correspond to the slip direction and slip plane normal of slip system $\alpha$, respectively. The elastic deformation gradient is calculated,

$$F^e = F \cdot (F^p)^{-1}, \tag{3}$$

to compute the elastic Green strain tensor,

$$E^e = \frac{1}{2}\left[(F^e)^T \cdot F^e - I\right], \tag{4}$$

This tensor is then multiplied by the fourth rank elasticity tensor with cubic symmetry, $C$, to compute the 2nd Piola–Kirchhoff stress,

$$\sigma^{PK2} = C : E^e \tag{5}$$

while the Cauchy stress is computed as,

$$\sigma = \frac{1}{det(F^e)}\left[F^e \cdot \sigma^{PK2} \cdot (F^e)^{-1}.\right] \tag{6}$$

The shearing rate on slip system $\alpha$ represents the probability of dislocation gliding and follows the Arrhenius-type flow rule proposed by Kocks et al. (1975),

$$\dot{\gamma}^\alpha = \dot{\gamma}_0^\alpha \exp\left(-\frac{F_0}{k_B T}\left\langle 1 - \left[\frac{\tau_{eff}^\alpha}{s_t^0 \frac{\mu}{\mu_0}}\right]^p \right\rangle^q\right) \mathrm{sgn}\left(\tau^\alpha - B^\alpha\right), \tag{7}$$

where $k_B$ is the Boltzmann constant, $F_0$ is the glide activation energy, $s_t^0$ is the thermal stress at $0K$, and $p$ and $q$ are profile parameters. Also, $\mu$ and $\mu_0$ are the shear modulus at temperature $T$ and $0K$ and the Macaulay brackets follows $\langle G\rangle = 0$ if $G \le 0$ or $\langle G\rangle = G$ if $G > 0$. The probability of gliding can be related to the shear rate along slip system $\alpha$ following Orowan's model, which computes the effective shearing rate ($\dot{\gamma}_0^\alpha$) as,

$$\dot{\gamma}_0^\alpha = \rho^\alpha b l_{struct} \nu, \tag{8}$$

where $\nu$ is the dislocation attempt frequency and $b$ is the Burger's vector. Furthermore, $l_{struct}$ corresponds to the dislocation mean free path, which varies for different crystals orientations and loading levels Devincre et al. (2008). Eq. (7) relates the local plastic shear rate induced by dislocation glide with the local effective stress, $\tau_{eff}^\alpha$, driving the dislocations. Both magnitudes are associated with atomic scale unit processes, but relates to the mesoscale (finite element) level shear stress, $\tau^\alpha$, i.e.,

$$\tau_{eff}^\alpha = \left\langle |\tau^\alpha - B^\alpha| - S^\alpha \right\rangle, \tag{9}$$

in which $S^\alpha$ corresponds to the local athermal stress and $B^\alpha$ to the intragranular back stress. The athermal stress is computed as the sum of the stress required to bow-out dislocations and the colinear dislocation–dislocation interaction strength Castelluccio and McDowell (2017),

$$S^\alpha = \alpha_{LE}\frac{\mu b}{2d_{struct}} + \mu b\sqrt{A_{ii}\rho^\alpha}, \tag{10}$$

in which $\alpha_{LE}$ and $A_{ii}$ are the dislocation line energy and colinear dislocation interaction coefficients, respectively, both of which characterize atomic scale unit processes. The mobile dislocations density ($\rho^\alpha$) evolves with the balance between dislocation multiplication, annihilation and cross slip such that (Castelluccio and McDowell, 2017),

$$\dot{\rho}^\alpha = \frac{k_{multi}}{b l_{struct}}|\dot{\gamma}^\alpha| - \frac{2y_s^{edge}}{b}\rho^\alpha|\dot{\gamma}^\alpha| + \nu_G\frac{d_{struct}}{d_0}\left(\phi_{cs}\sum_{\beta=1(\beta\neq\alpha)}^{N}\rho^\beta e^{\left(-V_{cs}^\alpha\frac{\frac{\mu b}{4\pi y_s^{screw}}-|\tau^\alpha - B^\alpha|}{k_B T}\right)} - (1-\phi_{cs})\sum_{\beta=1(\beta\neq\alpha)}^{N}\rho^\alpha e^{\left(-V_{cs}^\beta\frac{\frac{\mu b}{4\pi y_s^{screw}}-|\tau^\beta - B^\beta|}{k_B T}\right)}\right). \tag{11}$$

Here, $k_{multi}$ scales the number of dislocations produced after applying a certain plastic shear strain while $y_s^{edge}$ and $y_s^{screw}$ are the annihilation distances for edge and screw dislocations, respectively. The cross-slip efficiency parameter $\phi_{CS}$ quantifies the likelihood for dislocation annihilation while cross slipping and $V_{cs}$ represents cross slip activation volume.

The mean spacing of sessile dislocations walls, $d_{struct}$, follows the so-called similitude relation (Sauzay and Kubin, 2011; Kubin and Sauzay, 2016),

$$d_{struct} = K_{struct}\frac{\mu b}{max(\tau^\alpha)}, \tag{12}$$

in which $K_{struct}$ is a similitude coefficient. Castelluccio and McDowell (2017) further proposed to relate dislocations mean free path to $d_{struct}$,

$$l_{struct} = \eta d_{struct}, \tag{13}$$

where the substructure aspect ratio, $\eta$, is a mesoscale attribute that describes the dislocation structure morphology and depends on the crystallographic orientation and deformation (Lin et al., 2021).

The deformation of stiffer dislocation walls compared to the bulk results in an internal residual stress referred to as the intragranular back stress. Assuming an Eshelby elastic hollow inclusion Castelluccio and McDowell (2017) derived that the back stress rate follows,

$$\dot{B}^\alpha = \frac{f_w}{1-f_w}\frac{2\mu(1-2S_{1212})}{1+4S_{1212}f_{Hill}^S}\dot{\gamma}^\alpha, \tag{14}$$

in which the Hill factor, $f^S_{Hill}$, is defined as the instantaneous plastic deformation tangent, i.e

$$f^S_{Hill} = \frac{1}{2}\frac{d\gamma_p}{d\sigma}, \tag{15}$$

$f_w$ is the dislocation wall volume fraction and

$$S_{1212} = \frac{\pi\eta^2 + (\eta^2 - 1.75 - 2\nu_p\eta^2 + 2\nu_p)C_{12}}{8\pi(1-\nu_p)(\eta^2-1)} \tag{16}$$

is the Eshelby tensor component for a prolate spheroid (Mura, 1987) with

$$C_{12} = \frac{2\pi\eta(\eta\sqrt{\eta^2-1} - cosh^{-1}(\eta))}{,}\sqrt{(\eta^2-1)^3} \tag{17}$$

and

$$\nu_p = \frac{\nu + \frac{2}{3}\mu(1+\nu)f^S_{Hill}}{1 + \frac{4}{3}\mu(1+\nu)f^S_{Hill}}. \tag{18}$$

The model is fully defined once the mesoscale attributes $\eta$ and $f_w$ are computed as explained in the following section.

### 2.2. Mesoscale structure identification

Dislocation structures evolve during loading according to their relative stability. Early on Holt (1970) proposed that such a process can be assimilated to a spinodal decomposition. We follow a similar spirit to propose an approach in which structure transformations are analogous to phase transformations among the three stable structures described by Hansen et al. (2001, 2006). Hence, we assume that each type has intrinsic attributes $\eta^{\#}$ and $f^{\#}_w$ ($\# : I, II, III$) that characterize well developed structures (e.g., at 20% strain), while the partition and accumulation of plasticity modulate the transition through these states.

We hypothesize that the strength of the dislocation interactions (Hirth, 1961) determines the likelihood that a structure is stable. Hirth (1961) computed the relative interaction strengths for Hirth locks, Cottrell locks and cross slip as 0.66, 0.33 and $< 0.167$, respectively. We argue that the strength of Hirth locks impairs cross slip and results in elongated anisotropic cells from coplanar dislocation annihilation. Weaker Cottrell locks are less effective in preventing cross slip induced annihilation and result in more equiaxed structures compared to those dominated by Hirth locks. The absence of both these locks along with profuse cross slip results in fully equiaxed isotropic cells.

Upon loading, dislocation production, lock formation, and cross slip annihilation results in a gradual transition among structures. We can equate this response to a transition from coplanar dislocations (anisotropic and athermal) into cross slip dominated structures (equiaxed and thermal). We assume that the partition of plastic shear in the corresponding lock planes serves as a predictor for the transition among structures. The plastic shear partition refers to the accumulated shear strain on slip planes that form various locks or cross slip with respect to the most active slip plane. Hence, equiaxed cells (Type III) appear when the plastic shear strain on the cross slip plane associated to the most active slip plane exceeds the critical value $\gamma_{Cr}$. Similarly, Type I and II structures will appear depending on the relative accumulation of shear strain on planes that form Hirth or Cottrell locks, provided the cross slip threshold is not exceeded.

Fig. 1 summarizes the strategy to identify the dominant structure with a flowchart that depends on the equivalent shear strain ($\gamma^{eq}$),

$$\gamma^{eq} = \left(\gamma_{max} + \gamma_{Cottrell} - \frac{1}{2}\gamma_{Hirth}\right) \tag{19}$$

which corresponds to the weighted summation of the accumulated shear on the most active slip system and its corresponding Hirth and Cottrell slip systems. Also $\gamma^{eq}_0 \sim 10$ (Fig. 1) is the inverse of the typical equivalent shear strain upon reaching Stage III hardening, at which point $f_w$ and $\eta$ saturate and become constant (Muller et al., 1996; Estrin et al., 1998). Furthermore, the factor $\frac{1}{2}$ arises from the strength of Hirth locks being approximately twice of that for Cottrell locks. The dislocation wall volume fraction depends on the plastic strain accumulation across multiple slip plane and is computed as explained in Fig. 1. The error function is characteristic of smooth phase transformations (Porter, 1992) and modulates the roles of Hirth or Cottrell locks on preventing cross slip for Types I and II structure. These equations result in a delay in the transformation into equiaxed cells from Hirth locks while shear strains on slip planes associated with Cottrell locks accelerate it.

## 3. Parameter identification

To mitigate the lack of parameter uniqueness in crystal plasticity we seek a physics-based rather than a pure mathematical strategy (Sedighiani et al., 2022). In practice, parameter ambiguity arises from limited experimental data available to identify a large number of parameters. Thus, we mitigate this problem by integrating experimental data for multiple metals with identical mechanisms at similar homologous temperatures.

We further differentiate between low and high sensitivity parameters based on their expected modeling impact upon changes within their independent value bounds. In this sense, parameters with relatively low uncertainty or impact can be regarded as exact. However, atomic and mesoscale scale processes parameters that describe the response of a statistical ensemble are typically know with limited accuracy. For these high uncertainty parameters, we make an informed guess based on the value ranges reported on the literature.

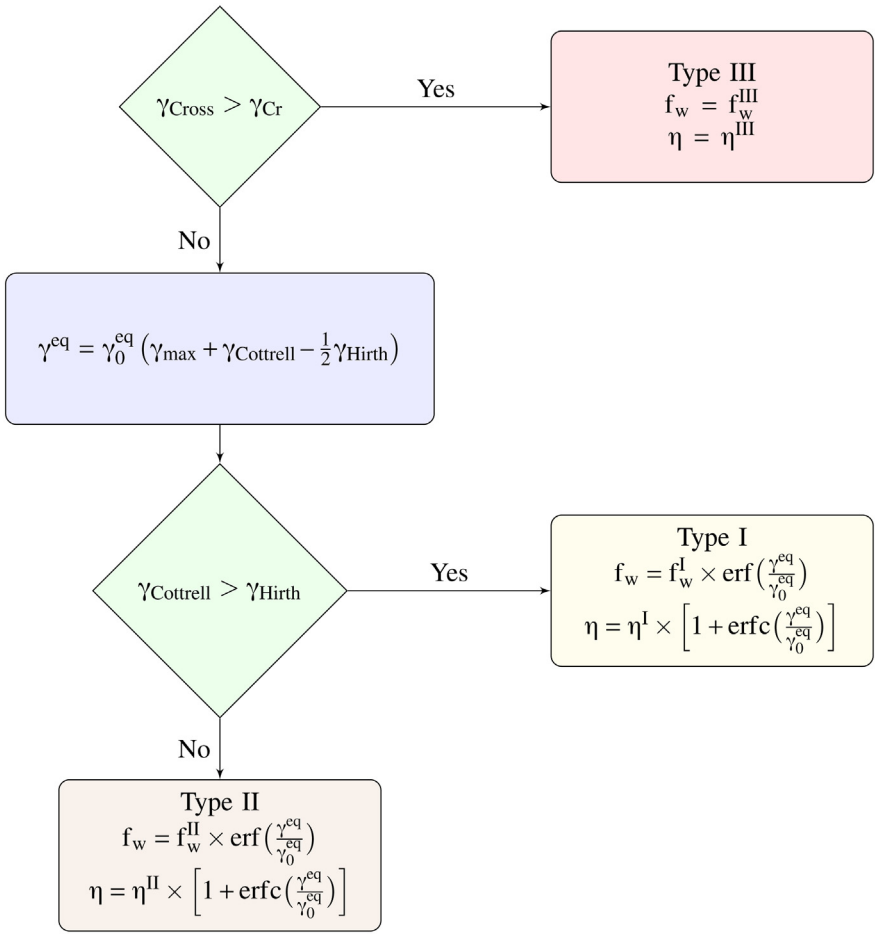


**Fig. 1.** Flowchart for the identification of mesoscale attributes $\eta$ and $f_w$. Type III structures (equiaxed cells) have constant wall fraction and aspect ratio, and they develop upon profuse cross slip from the dominant slip system. For Type I and II (elongated cells), $\eta$ and $f_w$ are modulated by error function. The accumulated shear strain on the most active slip system and on the slip planes that form Hirth and Cottrell locks control the evolution of the structures.
*Source:* TEM images adapted from Livingston (1962), Sard and Weil (1970).

**Table 1**
Parameters with low sensitivity for Al, Cu and Ni. The shear modulus and elastic constants were computed based on Vigot (Ledbetter and Naimon, 1974), and Varshni (1970) for Cu and Ni at 298 K and Al at 77 K.

| Parameter | Model inputs |
|---|---|
| Burgers vector, $b$, (Å) | 2.56 (Cu) 2.86 (Al) 2.49 (Ni) (Ashraf and Castelluccio, 2021) |
| Initial dislocation density, $\rho_0$, $(\frac{1}{m^2})$ | $10^8$ (Williamson and Smallman, 1956) |
| Initial wall spacing, $d_0$, (μm) | 12 (Williamson and Smallman, 1956) |
| Shear modulus at room temperature, $\mu$, (GPa) | 45 (Cu) 28 (Al) 80 (Ni) (Ledbetter and Naimon, 1974; Varshni, 1970) |
| Shear modulus at 0 K, $\mu_0$, (GPa) | 55 (Cu) 31.6 (Al) 92 (Ni) (Ledbetter and Naimon, 1974; Varshni, 1970) |
| Elastic constant, $C_{11}$, (GPa) | 161 (Cu) 115 (Al) 249 (Ni) (Ledbetter and Naimon, 1974; Varshni, 1970) |
| Elastic constant, $C_{12}$, (GPa) | 119 (Cu) 62 (Al) 155 (Ni) (Ledbetter and Naimon, 1974; Varshni, 1970) |
| Elastic constant, $C_{44}$, (GPa) | 75 (Cu) 31 (Al) 114.6 (Ni) (Ledbetter and Naimon, 1974; Varshni, 1970) |

### 3.1. Parameters with low expected sensitivity

The Burgers vector, $b$, the shear modulus at room and $0K$ temperature, $\mu$ and $\mu_0$, and the elastic constants, $C_{11}$, $C_{12}$, and $C_{44}$ are regarded as low uncertainty and low sensitivity. Similarly, we assume that the initial dislocation density, $\rho_0$, and initial wall spacing, $d_0$, correspond to those from well annealed materials (Williamson and Smallman, 1956). Table 1 summarizes the values from the low uncertainty parameters for Al, Cu and Ni.

**Table 2**
Atomic scale parameters considered in the crystal plasticity model.

| Parameter | Model inputs |
|---|---|
| Glide activation energy, $F_0$ ($\frac{\text{KJ}}{\text{Mole}}$) | 145 (Cu) 150 (Ni) 100 (Al) (Ashraf and Castelluccio, 2021) |
| Athermal stress at 0 K, $s_0^t$ (MPa) | 10 (Cu), 30 (Ni), 10 (Al) (Ashraf and Castelluccio, 2021) |
| The profile parameters, $p$ | 0.67 (Ashraf and Castelluccio, 2021) |
| The profile parameters, $q$ | 1.5 (Ashraf and Castelluccio, 2021) |
| The annihilation distances for edge dislocations, $y^s_{edge}$ (nm) | 2.0 (Cu) 2.0 (Ni)<br>4 (Al, 77 K) (Aslanides and Pontikis, 2000) |
| The annihilation distances for edge dislocations, $y^s_{screw}$ (nm) | 40.0 (Cu) 40.0 (Ni)<br>80.0 (Al, 77 K) (Feaugas, 1999) |
| The cross slip frequency, $\nu$ ($s^{-1}$) | $10^{12}$ (Castelluccio and McDowell, 2017) |
| Cross slip activation volume, $V^0_{cs}$ (MPa) | $1.67 \times 10^{-26}$ (Armstrong and Rodriguez, 2006) |
| Cross-slip efficiency parameter, $\phi$ | 0.5 (Castelluccio and McDowell, 2017) |

**Table 3**
Model mesoscale parameters used in the crystal plasticity model. All values are within the best independent guess from lower scale modeling and experiments.

| Parameter | Experimental range | Model inputs |
|---|---|---|
| The self-interaction coefficient, $A_{ii}$ | 0.1 to 0.3 | 0.1 (Fivel et al., 1998; Devincre et al., 2008) |
| The line tension, $\alpha_{LE}$ | 0.5 to 1.5 | 1.0 (Tabata et al., 1982; Szajewski et al., 2015) |
| The dislocation multiplication factor, $K_{multi}$ | 1 to 4 | 1.0 (Tabata et al., 1982; Castelluccio and McDowell, 2017) |
| Similitude coefficient, $K_{struct}$ | 5 to 10 | 8 (Sauzay and Kubin, 2011; Kubin and Sauzay, 2016) |
| Wall fraction - Type I , $f_w^I$ | 0.1 to 0.5 | 0.23 |
| Wall fraction - Type II , $f_w^{II}$ | 0.1 to 0.5 | 0.25 |
| Wall fraction - Type III , $f_w^{III}$ | 0.1 to 0.5 | 0.2 |
| Aspect ratio - Type I , $\eta^I$ | 1.0 to 5.0 | 4.0 |
| Aspect ratio - Type II , $\eta^{II}$ | 2.0 to 10.0 | 5.0 |
| Aspect ratio - Type III , $\eta^{III}$ | $\simeq 1.0$ | 1.0 |
| Equivalent shear strain coefficient, $\gamma_0^{eq}$ | 5–20 | 10 |
| Critical cross slip strain, $\gamma_{Cr}$ | – | $10^{-2}$ |

### 3.2. Atomic scale process parameters

The glide activation energy ($F_0$) and the thermal stress at 0 K ($s_0^t$) carry significant uncertainty associated with the thermal activation required for a dislocation to surpass an atomic-scale obstacle and enable glide. Ashraf and Castelluccio (2021) considered the change in yield stress with temperature to develop an independent parameterization of $F_0$ and $s_0^t$ for various materials, including Cu, Ni and Al. Similarly, atomistic and experimental analyses have estimated the annihilation distance for edge dislocations, $y^s_{edge}$, to be in the range between 0.5 to 5.0 nm at room temperature (Aslanides and Pontikis, 2000) while that for screw dislocations $y^s_{screw}$ is in the range of tens to hundreds of nanometers (Feaugas, 1999). Cross slip also depends on several parameters such as the jump frequency, $\nu_G = 10^{12}\ s^{-1}$ (Castelluccio and McDowell, 2017) and the activation reference volume, $V^0_{cs} = 1000b^3$ (Armstrong and Rodriguez, 2006). Table 2 summarizes the values of atomic scale parameters used in the model.

### 3.3. Mesoscale parameters

We now consider parameters associated with the line and structure character of dislocations, which are summarized in Table 3. All parameters fall within the range from independent estimations using models and experiments. For example, the colinear dislocation interaction coefficient, $A_{ii}$, has been estimated by numerous experiments and dislocation dynamic simulations (Fivel et al., 1998; Devincre et al., 2008) to be between 0.1 to 0.15. Sauzay and Kubin (2011), Kubin and Sauzay (2016) also analyzed the similitude coefficient, $K_{struct}$, and concluded it has a value between five and ten under monotonic loading for a wide range of FCC metals. Similarly, the line tension, $\alpha_{LE}$ is associated with the stress required to create new dislocations and has been estimated in the range of 0.5 to 1.5 (Tabata et al., 1982; Szajewski et al., 2015). Furthermore, the dislocation multiplication factor, $K_{multi}$, has been estimated in the range between one to four by Tabata et al. (1982) and between one and two by Castelluccio and McDowell (2017).

Following an extensive characterization of structures from TEM images for various FCC metals (see Appendix A), we estimated the intrinsic $\eta^{\#}$ and $f_w^{\#}$ for each type of structure. The results in Fig. 2 demonstrate that Type II structures are the most anisotropic and correspond to elongated cells typically with $3 < \eta^{II} < 10$ as a result of strong Hirth locks. Type I structures are controlled by weaker Cottrell typically with $1 < \eta^{I} < 5$. In the absence of these locks along with profuse cross slip across result in fully equiaxed cells (Type III, $\eta^{III} \simeq 1.0$).

Similarly, we evaluated the wall fraction parameter for each structure type and concluded that in all cases $f_w$ is in the range between 0.2 to 0.25 for homologous temperatures in between 0.1 to 0.2. Upon enough straining (e.g., Stage III of hardening), cross slip will be activated and structures will evolve towards more equiaxed cell structures of Type III. For a fix applied strain, the critical cross slip strain, $\gamma_{Cr}$, controls the boundary that transitions into cells as shown by Fig. 3. By decreasing $\gamma_{Cr}$, a larger fraction of the inverse pole figure develops cells.

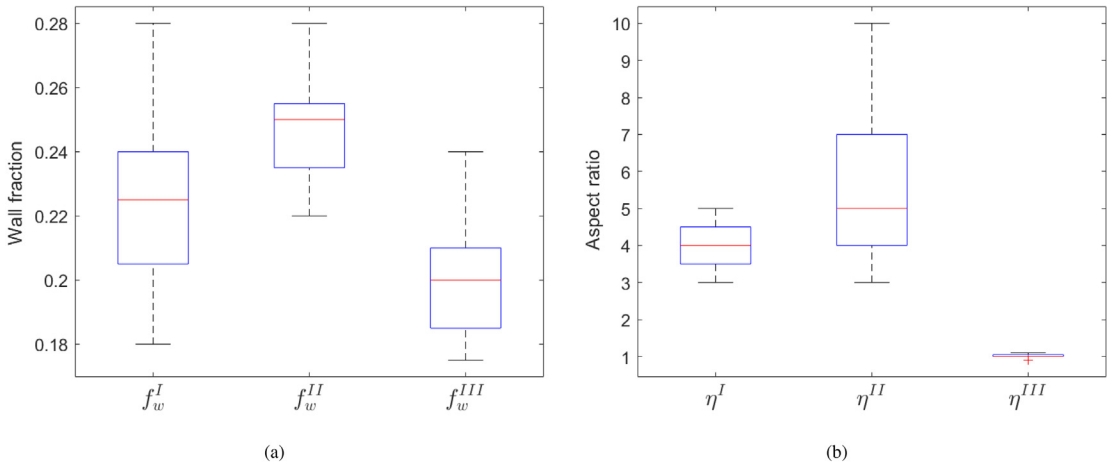


**Fig. 2.** Characteristic mesoscale attributes of dislocation structures estimated from TEM images for Cu as explained on Appendix A: (a)Wall fraction ($f_w$) and (b)Aspect ratio ($\eta$). The plots correspond to a minimum of ten measurements.

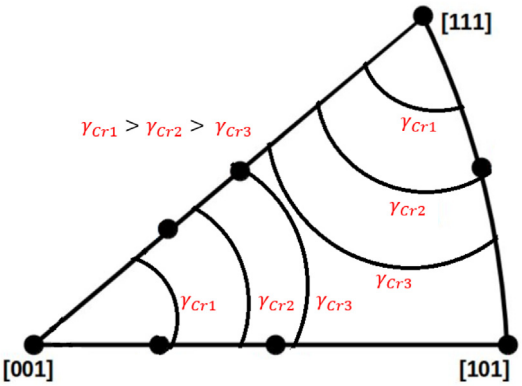


**Fig. 3.** Schematic representation of the effect of $\gamma_{Cr}$ on transitioning into Type III structures. The lines corresponds to the boundary that delimit the orientations that results in cells at a fixed straining level. Upon further loading, lines moves towards single slip at the center.

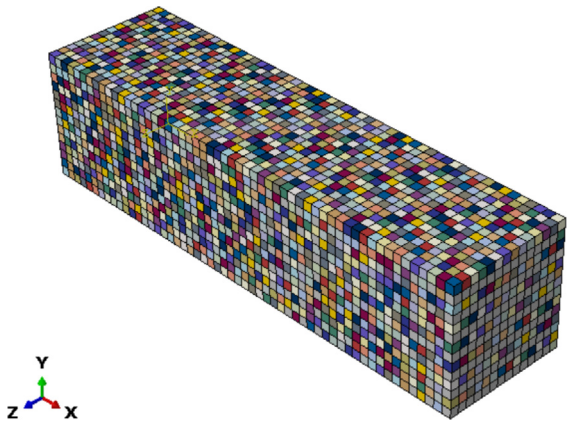


**Fig. 4.** Finite element mesh with ten thousand elements and uniaxial boundary conditions. Pictorial description of different grains indicated with different colors (no correlation with Euler angles values).

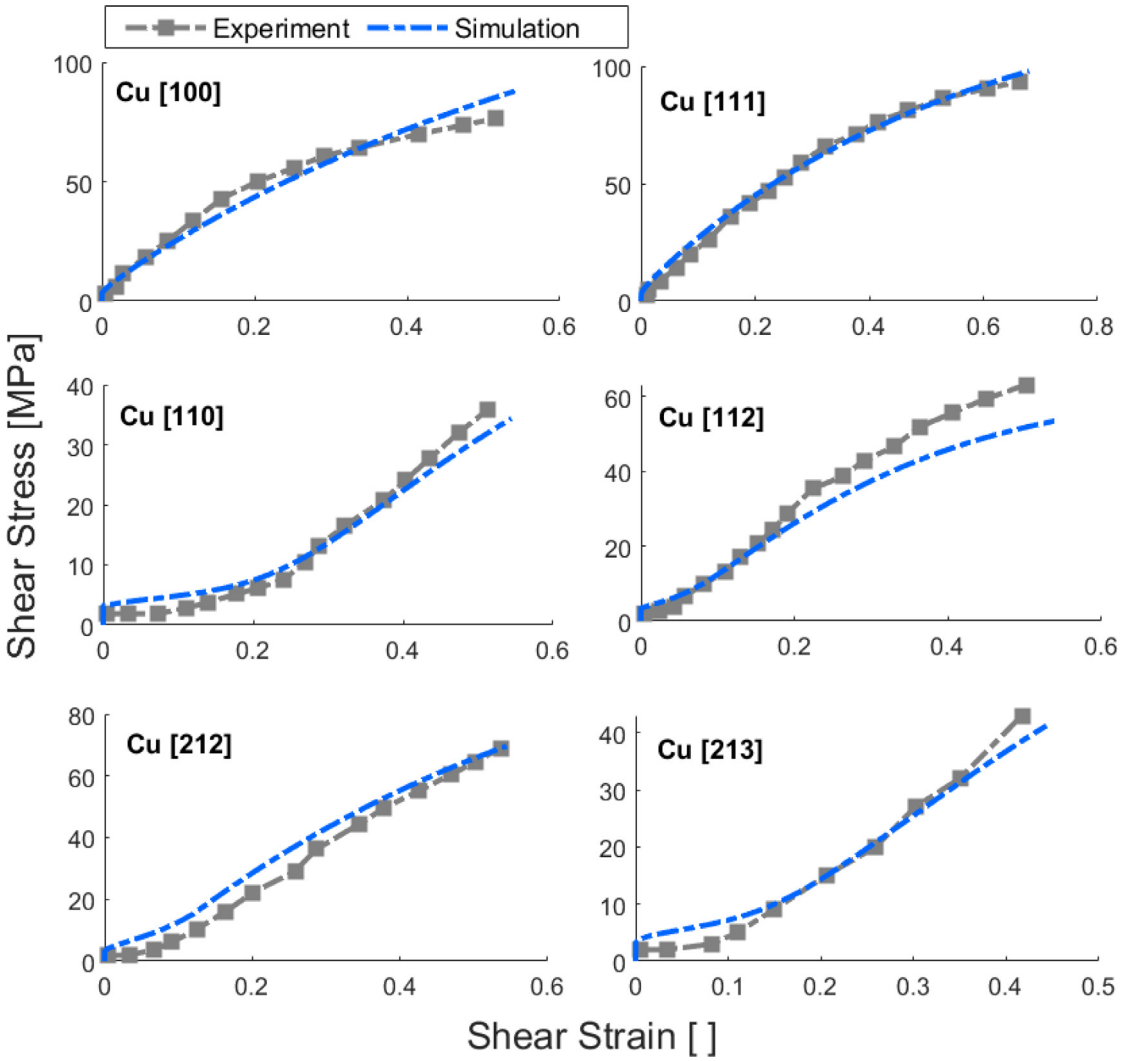


**Fig. 5.** Comparison of the shear stress-shear strain curve of Cu single crystals from models and experiments.
*Source:* Experimental data taken from Takeuchi (1975).

### 3.4. Finite element implementation

The model was implemented in Abaqus 2020 (Anon, 2020) making use of the user material subroutine (UMAT) and an 8-node linear brick mesh with reduced integration and hourglass control (C3D8R). Single crystal simulations one element and polycrystalline simulations consider ten thousand elements (Fig. 4), which suffice to represent the macroscopic stress–strain response (Han et al., 2020). Each element is randomly oriented according to the distribution produced by MTEX (Hielscher and Schaeben, 2008) and grain boundaries are assumed impenetrable. Straining corresponds to displacing the back face of the mesh along the $X$-axis while the front face is constrained and displacements are allowed along $Y$-axis and $Z$-axis directions. Appendix B further considers different polycrystalline models with realistic microstructure and equiaxed grains.

Following the numerical integration scheme proposed by McGinty (2001), the algorithm solves Eq. (7) with an implicit solution for each integration point at each time increment. The resolved shear stress, the back stress, and the athermal stress all depend on the values of $\dot{\gamma}^{\alpha}$ and they are solved simultaneously by a Newton–Raphson method (McGinty, 2001) that defines the slip system level function,

$$f^{\alpha} = \dot{\gamma}^{\alpha} - \dot{\gamma}_0^{\alpha} \exp\left( -\frac{F_0}{k_B T} \left\langle 1 - \left[ \frac{\left\langle \left| \tau_{eff}^{\alpha} \right| \right\rangle}{s_i^0 \frac{\mu}{\mu_0}} \right]^p \right\rangle^q \right) \operatorname{sgn}\left( \tau_{eff}^{\alpha} \right), \tag{20}$$

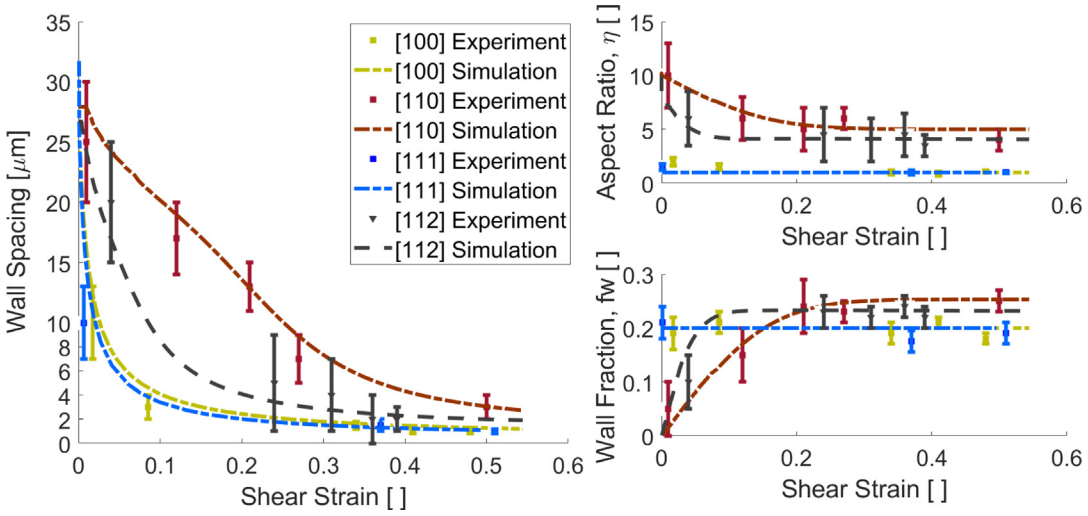


**Fig. 6.** Comparison of mesoscale attributes from models and experiments for Cu crystals. *Source:* Experimental data taken from Ambrosi et al. (1974), Huang et al. (2001), Livingston (1962), Mughrabi et al. (1986), Sumino et al. (1963).

in which the values of $\dot{\gamma}$ that minimize $f^{\alpha}$ correspond to the solution of this non-linear systems of equations. The Newton–Raphson computes the unknown $\dot{\gamma}$ by iteratively solving the equation system,

$$-\sum_{\beta=1}^{N_{sys}} \frac{\partial f^{\alpha}}{\partial \dot{\gamma}^{\beta}} \Delta\dot{\gamma}^{\beta} = f^{\alpha}. \tag{21}$$

along with the explicit integration of the back stress and dislocation density evolution (Eqs. (11) and (14)) with a sub-incrementation scheme (McGinty, 2001).

Next, the algorithm computes plastic velocity gradient for the next time increment,

$$L^{p}_{\Delta t} = \sum_{\alpha=1}^{N_{sys}} \dot{\gamma}^{\alpha}_{\Delta t}(s^{\alpha} \otimes m^{\alpha}), \tag{22}$$

and the plastic deformation gradient in the next time increment following,

$$F^{p}_{t+\Delta t} = exp(L^{p}_{\Delta t}\Delta t)F^{p}_{t}, \tag{23}$$

in order to compute the stress in the next time increment

$$\sigma_{t+\Delta t} = \frac{\left[F_{t+\Delta t}\cdot\left(F^{p}_{t+\Delta t}\right)^{-1}\cdot \boldsymbol{C} : \frac{1}{2}\left[(F_{t+\Delta t}.(F^{p}_{t+\Delta t})^{-1})^{T}\cdot F_{t+\Delta t}.(F^{p}_{t+\Delta t})^{-1} - I\right]\cdot\left(F_{t+\Delta t}\cdot\left(F^{p}_{t+\Delta t}\right)^{-1}\right)^{-1}\right]}{det\left(F_{t+\Delta t}\cdot\left(F^{p}_{t+\Delta t}\right)^{-1}\right)}. \tag{24}$$

## 4. Modeling results for single- and poly-crystals

We first present the results for six Cu single crystals deformed under monotonic loading at a strain rate of 0.2 $s^{-1}$ and 298 K in Fig. 5. Compared to the experimental results from Takeuchi (1975), the model closely approximates stress–strain responses for all hardening stages. We highlight that these results validate the model from multiple orientations covering the three types of structures.

A key aspect for the robustness of the current model is the multiscale parameterization, which implies that the model can reproduce the macroscopic stress strain curves and also mesoscale attributes such as morphology, size and wall fraction. To validate this aspect, we evaluated TEM images at various strain levels and obtained ten measurements for the wall spacing, aspect ratio and wall fraction following the procedure on Appendix A. Fig. 6 compares the evolution of the wall spacing, wall fraction and aspect ratio of dislocation structures computed from models and experiments. Overall, the model reproduces qualitatively and quantitatively the general mesoscale response and supports the value of independent parameterization of dislocation structures for modeling crystal response.

Given that mesoscale dislocation structures are common for FCC materials, we argue that our approach should be amenable to predict various material responses without adjusting mesoscale parameters. This property would grant excellent predictive power to represent the response of single- and poly-crystals for other materials with similar mesoscale structures, even when single crystal

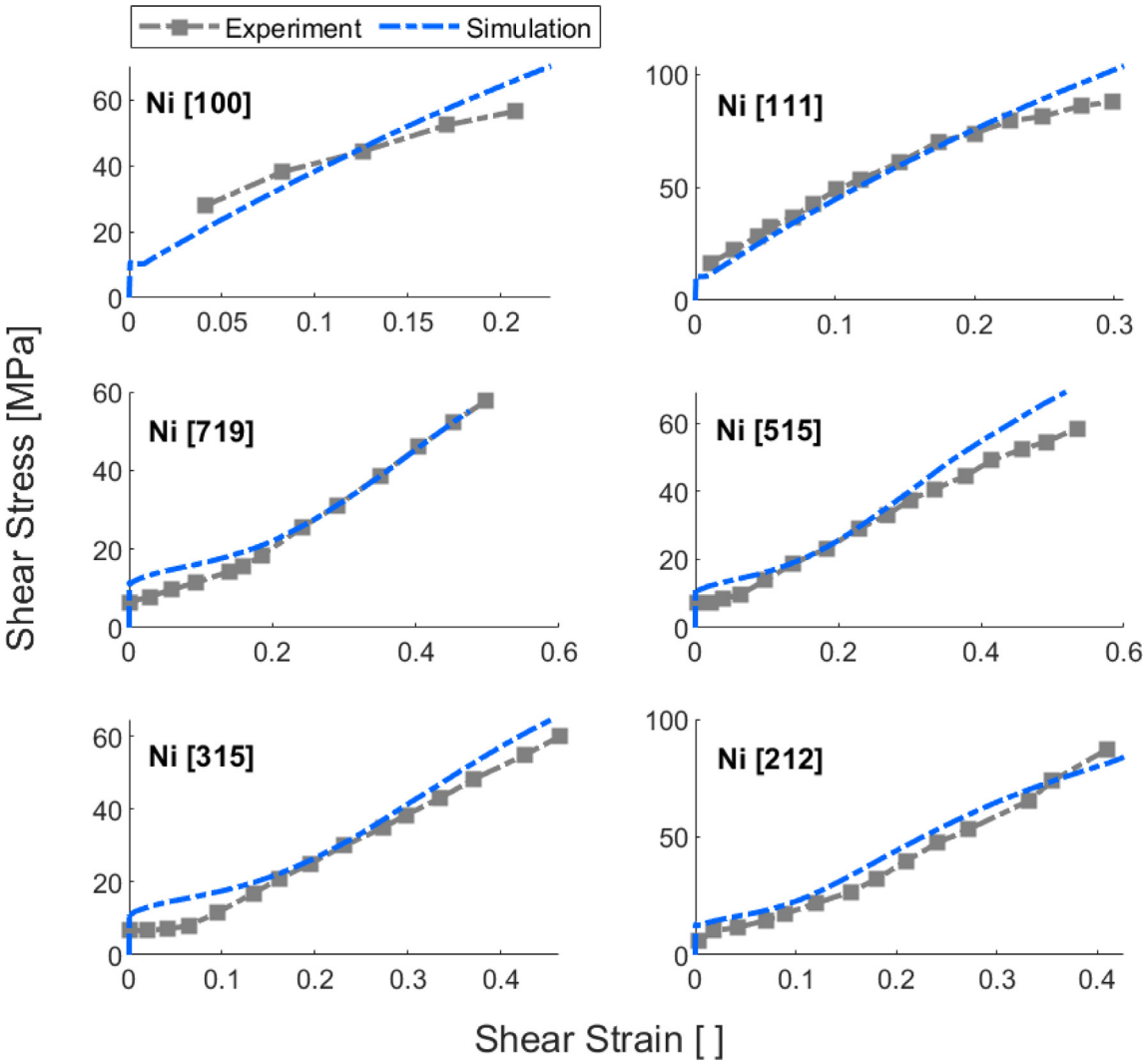


**Fig. 7.** Comparison of the shear stress-shear strain curve of Ni single crystals from models and experiments.
*Source:* Experimental data taken from Venkatesan and Beshers (1970), Follansbee and Gray (1991).

data is not available, such as for austenitic stainless steel (Anon, 2021; Li et al., 2019) or high entropy alloys (Lu et al., 2021; Zhu et al., 2018). Hence, we implemented the model for Ni at 298 K and Al at 77 K (0.1 to 0.2 homologous temperature) using identical mesoscale parameters. Figs. 7 and 8 present remarkable agreement considering that much of the hardening arising from dislocation structures was parameterized for Cu.

Since the single crystal model does not take into account crystal size effects, a fair comparison with polycrystals requires grain sizes large enough not to affect the dislocation mean free path. Hence, we compare to experiments with large grains and limiting the maximum dislocation mean free path to the average grain size. The results for polycrystals in Fig. 9 present excellent agreement between models and experiments. The model and the parameters are the same as those used for modeling single crystals, which reinforces the notion that matching single crystals provides good predictive power for polycrystals when grain size effects are not dominant. Fig. 10 further presents the equivalent the stress–strain response from each grain in the Cu simulation. Notably, the model results in significant variability among grains with the equivalent stress ranging from 0 MPa to 600 MPa at 25% deformation.

## 5. Discussion

We have presented a crystal plasticity constitutive model that, for the first time, predicts the monotonic response of a large number of single crystal and polycrystals from various metals using a single model. The model relies on identifying mesoscale attributes by surveying the partition of plastic deformation among slip planes and can be applied to single and polycrystals

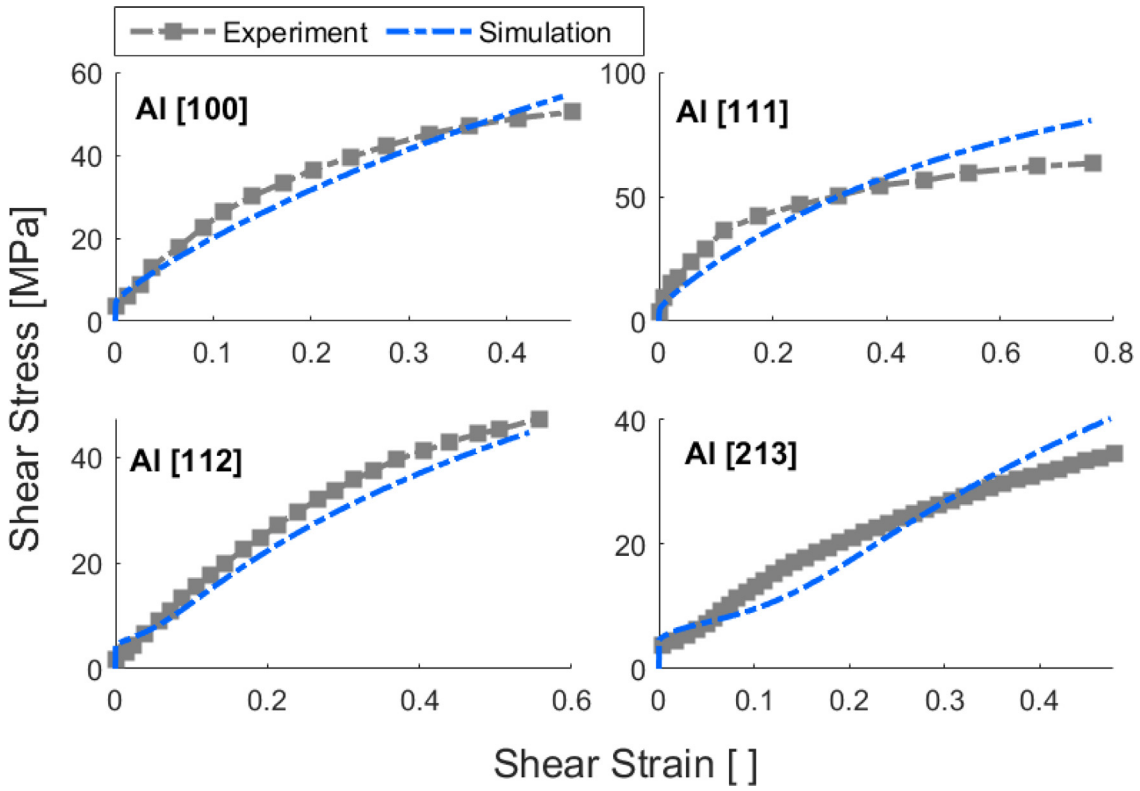


**Fig. 8.** Comparison of the shear stress-shear strain curve of Al at 77 K single crystals from models and experiments. *Source:* Experimental data taken from Mukherjee et al. (1965), Tagami et al. (2001).

indistinctly. The predictive power at the macroscopic scale is conferred by the independent validation of atomic- and meso-scale attributes.

By leveraging on TEM images and simulations we demonstrated that mesoscale parameters are identical (within the known certainty) among materials with similar structures. We have further quantified these *material-invariant* parameters (e.g., $A_{ii}$, $f_w$, $\eta$) confidently, which reduces the number of large uncertainty parameters. Hence, future applications of this crystal plasticity model should employ similar mesoscale parameters values along with an independent estimation of the atomic scale processes parameters (Table 2). We emphasize that models with parameters that can be estimated independently yield better predictive results compared to the simultaneous fitting of multiple parameters using polycrystalline experimental data.

### 5.1. Lack of predictive power from polycrystal parameter fitting

Several sets of parameters may predict the polycrystal behavior, but not all (if any) may reproduce single- and poly-crystal responses simultaneously. To exemplify this, we employed the mesoscale parameters in Table 4 to match the response of polycrystalline Cu (all other parameters still follow those in Table 1, Table 2, and Table 3). The three different sets of parameters result in good agreement between models and experiments as shown by Fig. 11. However, when applied to single crystals, Fig. 12 demonstrates that not all parameters are capable of predicting their responses. Notably, the error in predicting the stress reaches 100% for high Schmid factor crystals. Such large discrepancies at the crystal level demonstrate the limitations of parameterizations with polycrystalline experiments and explains the limited success of those crystal plasticity models in predicting the local crystal response.

### 5.2. Implications of anisotropic mean free paths

Next, we explore the role of the dislocation mean free path on the response of single crystals. Devincre et al. (2008) employed dislocation dynamics to demonstrate that the glide of dislocations is strongly anisotropic. Our approach indeed conveys this idea by assuming that the mean free path relates to the aspect ratio of each dislocation structure, which can be measured in experiments

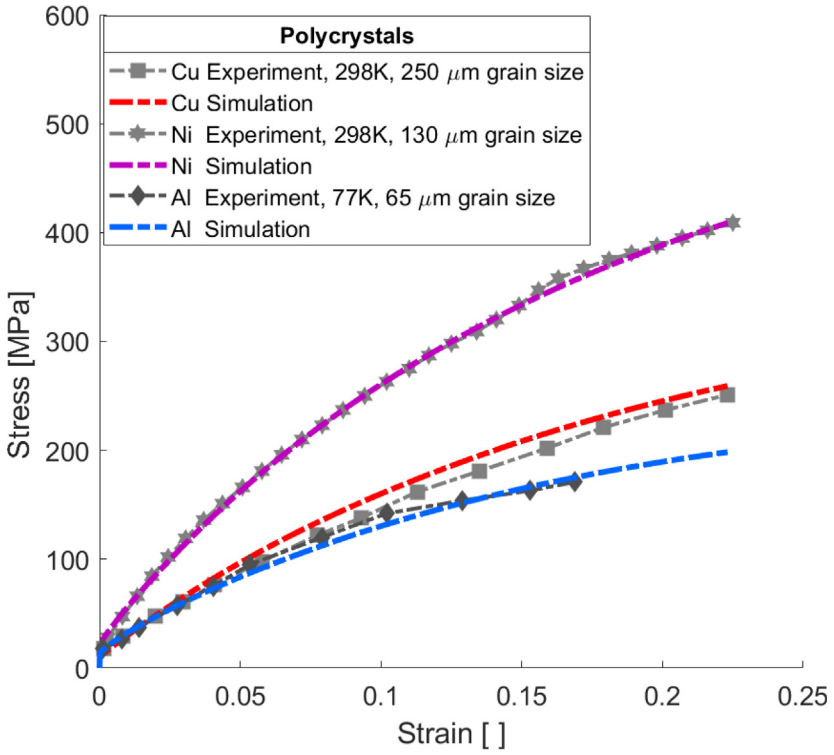


**Fig. 9.** Simulation results for polycrystalline Cu, Ni and Al with the same l parameters as for single crystals. *Source:* Experimental data taken from Carreker and Hibbard (1953), Gracio et al. (1989), Thompson (1977).

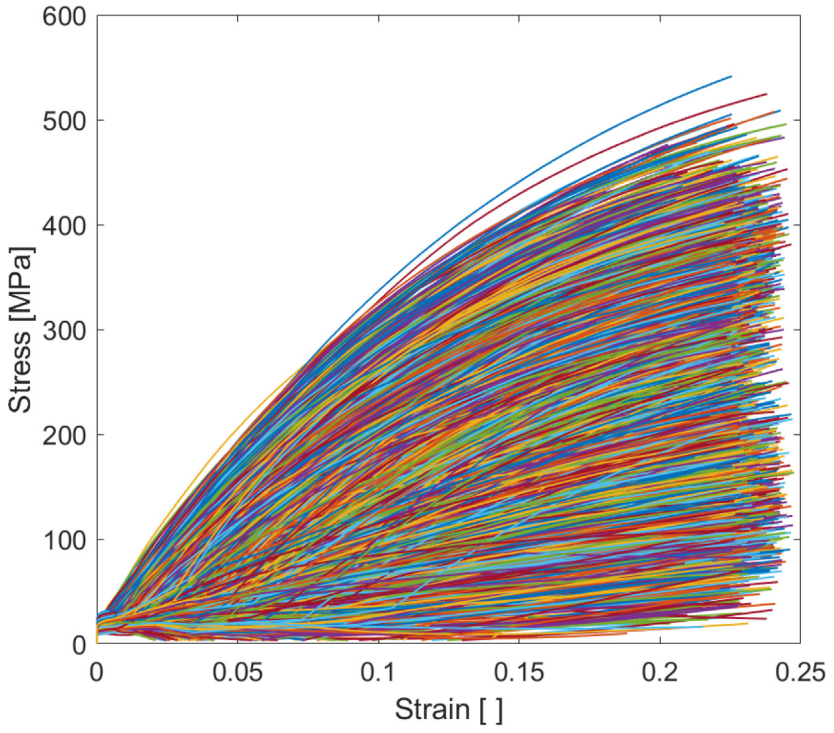


**Fig. 10.** Equivalent stress–strain response from ten thousand grains from Cu polycrystal simulation.

**Table 4**
Three parameter sets for Cu recreated to demonstrate that matching polycrystals does not guarantee good predictability of single crystals. Remaining parameters correspond to those in Tables 1, 2, and 3.

| Parameter | Set I | Set II | Set II |
|---|---|---|---|
| Wall fraction for Type II , $f_w^{II}$ | 0.25 | 0.2 | 0.1 |
| Elongated structure aspect ratio for Type I , $\eta^I$ | 3.5 | 3.0 | 6.0 |
| Similitude coefficient, $K_{struct}$ | 9.0 | 8.0 | 7.0 |

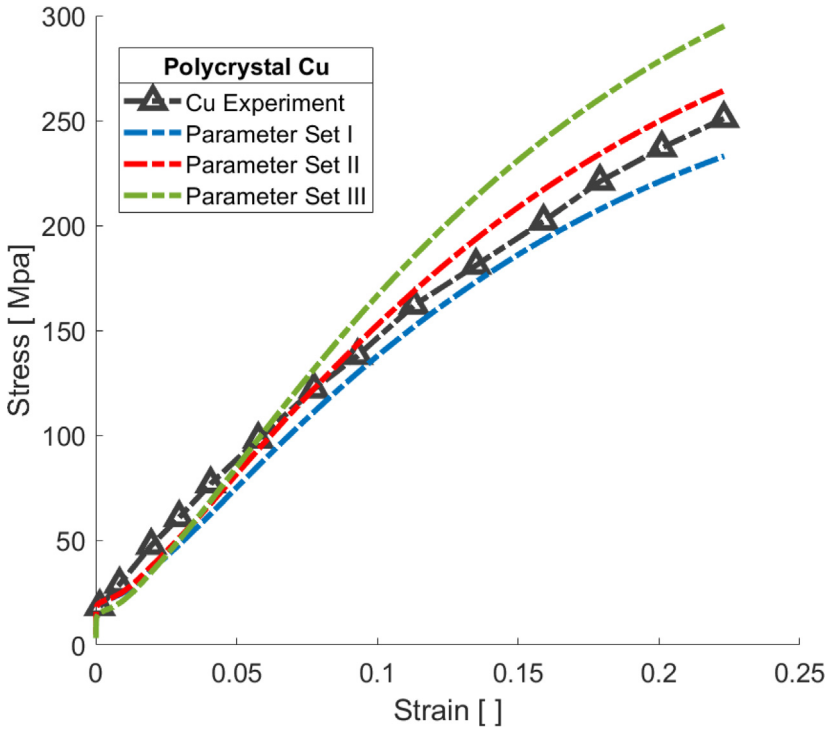


**Fig. 11.** Results for polycrystalline Cu using different sets of parameters of Table 4. Acceptable agreement with experiment is achieved despite the differences on the parameters.
*Source:* The experimental data is taken from Gracio et al. (1989).

with relatively low uncertainty. A different and popular approach (Alankar et al., 2011; Sedighiani et al., 2020) relates the mean free path to the square root of the dislocation densities. For instance, Wang et al. (2016) computed the dislocation mean free path,

$$l = \frac{1}{\sqrt{\alpha' \rho^{\alpha}}}, \tag{25}$$

with $\alpha' = 0.005$. We regard this formulation as harder to validate given the experimental uncertainty for quantifying dislocation densities.

To understand the role of the mean free path anisotropy, we implemented two model variations using a constant aspect ratio (Castelluccio et al., 2021a) with $\eta = 1.4$ or Eq. (25); All other aspects of the model remain the same as well as the same mesh and grain orientations used for polycrystalline simulations in Figs. 9 and 10. Fig. 13 confirms that both modifications still result in good agreement with the polycrystal experimental curve. However, Fig. 14 demonstrates that the modifications cannot predict the single crystal responses. Indeed, a constant structure aspect ratio or Eq. (25) result in fairly isotropic responses with all single crystals having almost the same response.

Fig. 15 further presents the corresponding equivalent stress–strain curves for all ten thousand grains in the polycrystalline simulation. Compared to the results in Fig. 10, the local variability in polycrystalline samples is drastically underpredicted when considering isotropic mean free paths ($\eta = 1.4$). These results further demonstrate that Eq. (25) also underpredicts the glide anisotropy and has intrinsic limitations in predicting the local response. For identical polycrystalline samples, our mesoscale model

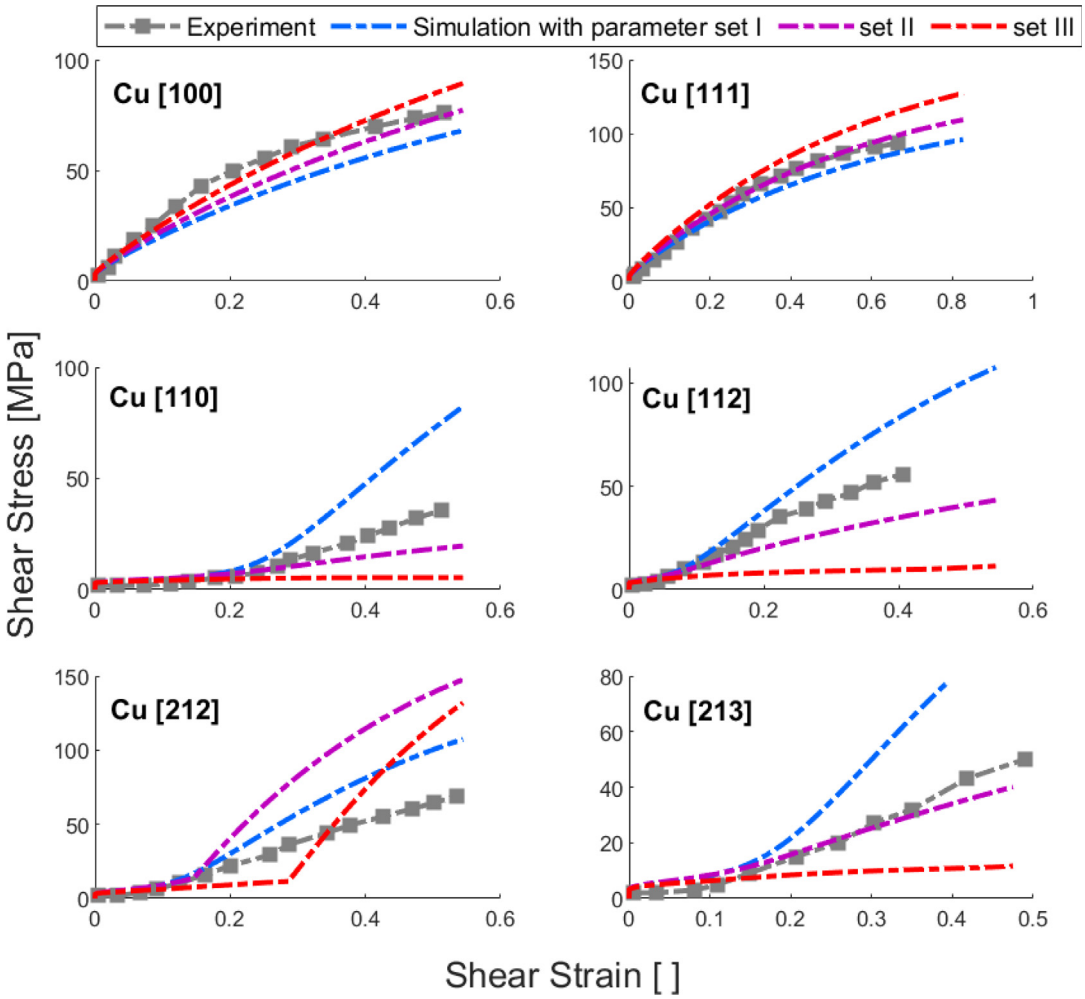


**Fig. 12.** The shear stress-shear strain curve of Cu crystals with different artificial sets of parameters in Table 4. The sets of parameters predict polycrystal (Fig. 11) but fail to predict single crystal responses.
*Source:* Experimental data is taken from Takeuchi (1975).

predicts a maximum equivalent stress at the grain level 50% higher than those predicted with Eq. (25). These miscalculations do not affect the average polycrystal response, but reduce the predictive power for single crystals and have important detrimental impact in damage prognosis. For example, the assessment of intergranular damage (Liang et al., 2021; Nicolas et al., 2019) often requires the quantification of the local stress at grain boundaries, which can hardly be predicted with isotropic models. This scenario requires a mesoscale validation linked to the stress, which in our case is provided by the similitude principle and cannot be replaced by grain-level strain measurements.

### 5.3. Further modeling advances

Our current approach has demonstrated a physic-based strategy to identify parameters with experimental information for various materials. Further research efforts can provide additional physical bases for the error function modulating mesoscale parameters as well as the critical cross slip shear strain ($\gamma_{Cr}$). We also envision novel material-invariant models that account for other hardening mechanisms arising from precipitates and twining in BCC and HCP materials.

We also note that the current model only convey size effects by limiting the mean free path and affecting the dislocation densities (Keller and Hug, 2017), which corresponds to isotropic hardening. However, size effects are often found predominantly on the back stress (Sato et al., 2012), which can be modeled by an explicit dependence on grain size (Kakandar et al., 2020; Castelluccio et al., 2021b) or strain gradient theories (Evans and Hutchinson, 2009). However, both approaches lack the physical understanding

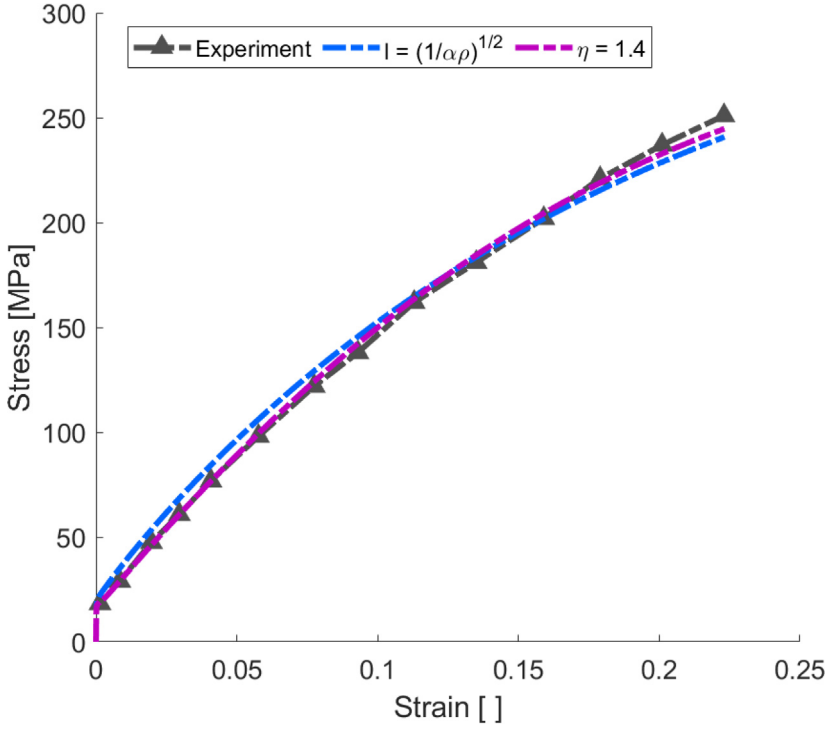


**Fig. 13.** Polycrystalline Cu stress strain curves with $\eta = 1.4$ ($l_{struc} = d_{struc}$) and Eq. (25). The agreement of the model result with experiment shows that the models predict well polycrystals stress strain response.
*Source:* The experiment from Gracio et al. (1989).

to estimate size-effect-related parameters independently. Hence, further efforts should integrate these approaches seeking meaningful understanding of their parameters and independent estimation.

Another area that deserves further exploration is the role of temperature on the response of crystals. Eq. (7), explicitly depends on temperature, but implicitly assumes that the glide activation energy, the thermal stress and the profile parameters do not depend on the temperature. On the contrary, some parameters such as elastic constants or the annihilation distances depend on temperature, both of which have been describe on the literature. Regarding mesoscale parameters, our recent analysis (Ashraf and Castelluccio, 2022) of dislocations structures under cyclic loading suggests that parameters associated with cells are temperature independent. As a results, parameters associated to Type III mesoscale are likely to be athermal.

## 6. Conclusions

This work introduced a physics-based crystal plasticity model based on mesoscale dislocation substructures that are observed in experiments. The model is designed so that all parameters and their uncertainty can be estimated independently from the macroscopic mechanical response, which enables multiscale validation. As a result, the model successfully predicts the monotonic mechanical response of single- and poly-crystals of FCC materials.

The model has been validated by comparing with the experimental stress strain curves from 16 single crystals and three polycrystals. In addition, the model correctly predicts the dominant dislocation substructures attributes (size, shape) as compared to those depicted by TEM images.

By characterizing mesoscale dislocation structures that are common for FCC materials, the approach can predict the mechanical response of various materials without modifying mesoscale parameters. This strategy grants a model excellent predictive power to represent the response of single- and poly-crystals for other materials with similar mesoscale structures, even when single crystal data is not available.

Finally, we demonstrated the importance of anisotropic mean free path formulations to predict the local response of single and polycrystals. We demonstrated that the models with more isotropic parameterizations of the mean free paths fail to predict single crystals and reduce the local variability, which is detrimental for damage prognosis.

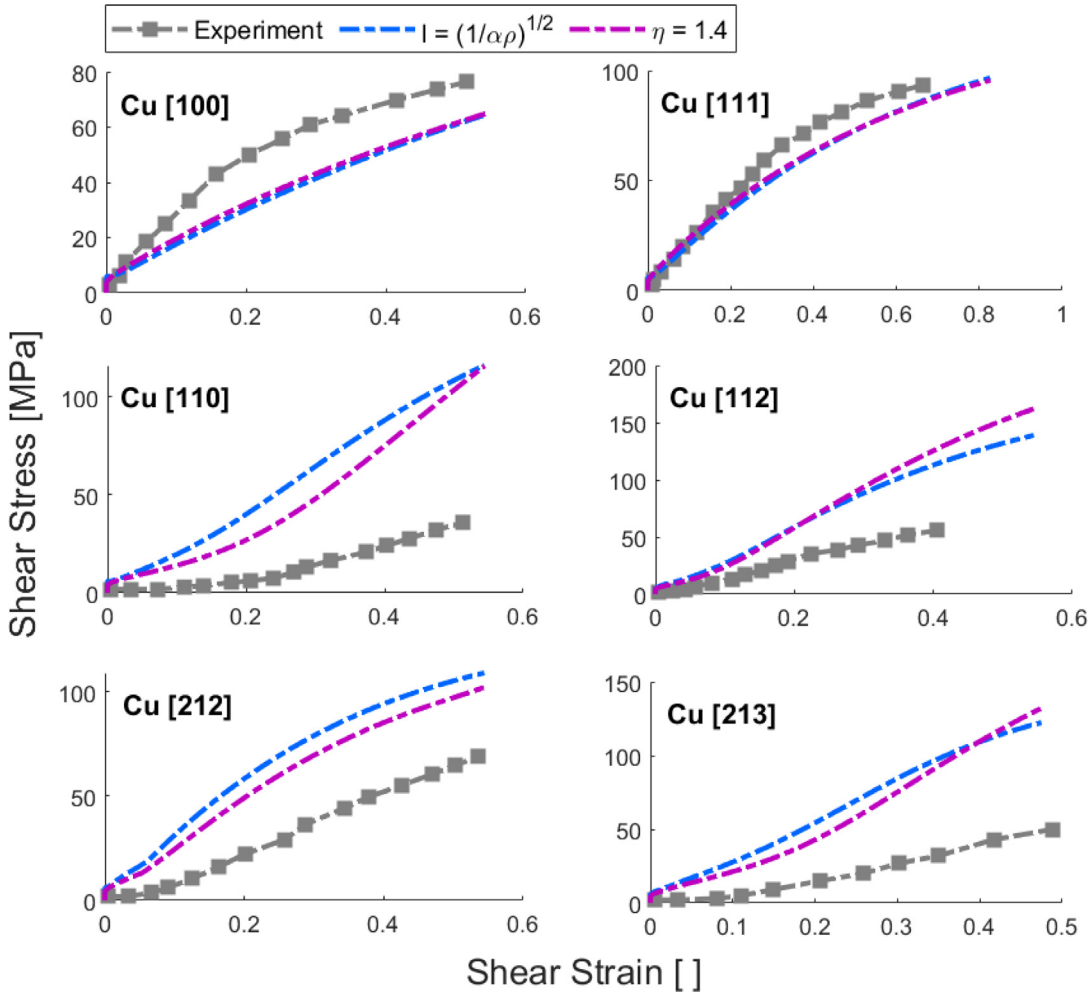


**Fig. 14.** The shear stress-shear strain curve of Cu single crystals with isotropic dislocation mean free path ($l_{struc} = \eta\ d_{struc}$, $\eta = 1.4$) and Eq. (25). While these condition well predicts polycrystal, Fig. 13, but fails to predict single crystals.
*Source:* The experiments from Takeuchi (1975).

## CRediT authorship contribution statement

**Shahram Dindarlou:** Performed the modeling, Data curation, Analysis, Manuscript preparation. **Gustavo M. Castelluccio:** Conceptualization, Methodology development, Funding acquisition, Manuscript preparation.

## Declaration of competing interest

The authors declare that they have no known competing financial interests or personal relationships that could have appeared to influence the work reported in this paper.

## Data availability

The authors confirm that the data supporting the findings of this study are available within the article or supplementary material.

## Acknowledgment

The authors are grateful for the support from EPSRC, UK Grant EP/R034478/1.

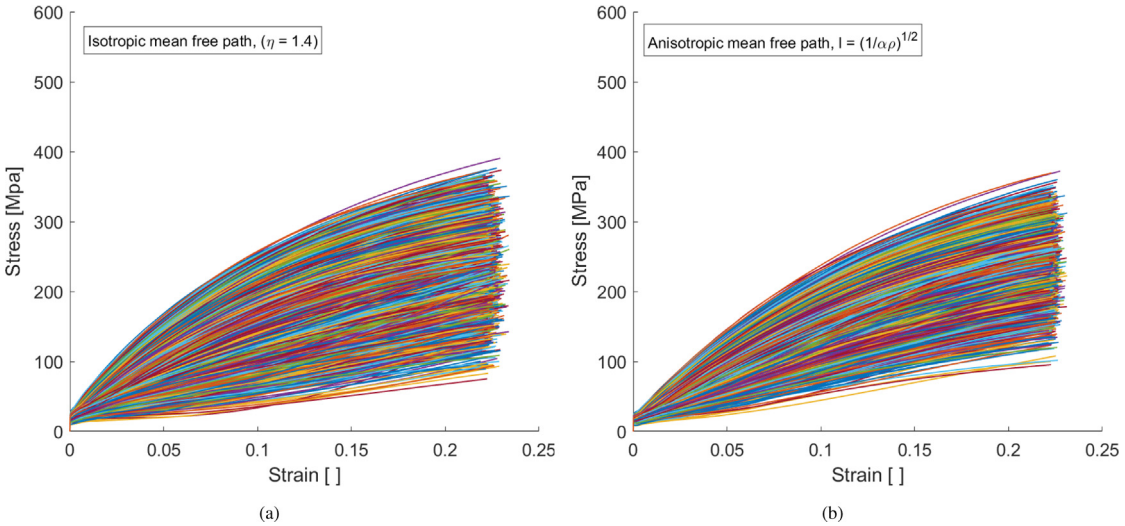


**Fig. 15.** Grain-level equivalent stress–strain response for ten thousand grains in the polycrystalline Cu model using (a) $\eta = 1.4$ and (b) Eq. (25). Compared to Fig. 10, the local variability is underpredicted by isotropic mean free paths models.

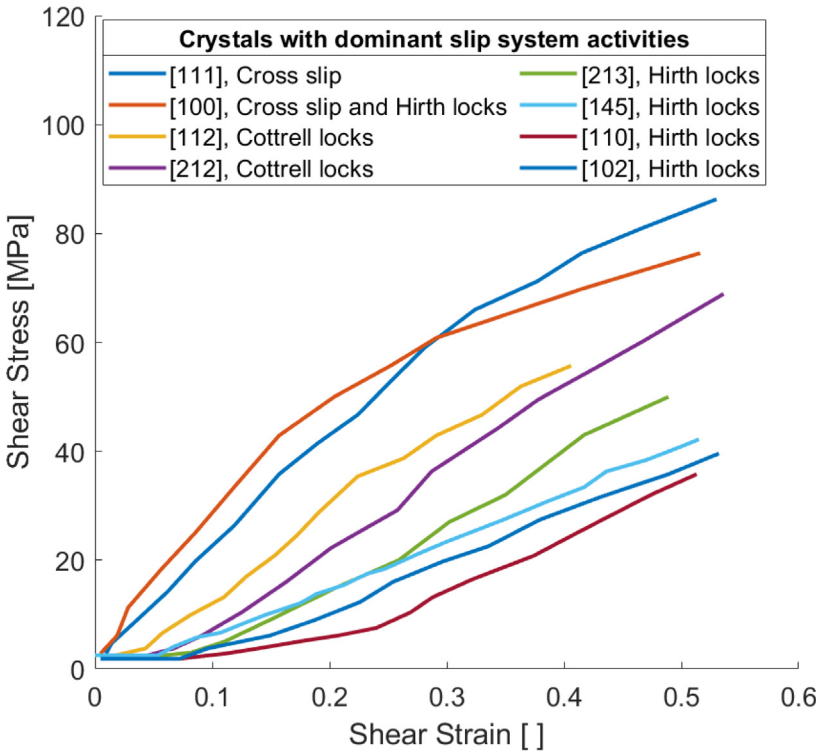


**Fig. A.16.** Experimental stress strain curves of Cu single crystals, three types of behavior are apparent. Each behavior type corresponds to a characteristic dominant dislocation activity, i.e, cross slip, Cottrell locks and Hirth locks (by performing a plasticity partitioning analysis, i.e, dividing the total strain by Schmid factor). For the crystals with two dislocation activity on the image, the first one is dominant. Although, for each dominant dislocation activity, a characteristic type of dislocation substructure exist from TEM images: equiaxed cells for cross slip, semi-elongated cells for Cottrell locks and elongated cells for Hirth locks.
*Source:* The strain stress curves from Takeuchi (1975), Steeds (1966), Kawasaki (1974).

## Appendix A. Experimental mesoscale attributes

By leveraging on extensive TEM images on the literature we estimated the mesoscale parameters for the three types of dislocation structures. Fig. A.16 shows experimental stress strain curves for Cu single crystals, which are dominated by three characteristic

100 Cu Crystal at 0.17 deformation, RT

| Cell No. | Dislocation structure attributes | | | |
|---|---|---|---|---|
| | D ($\mu m$) | t ($\mu m$) | $f_w = t/D$ | $\eta$ |
| 1 | 1.5 | 0.26 | 0.17 | 1.1 |
| 2 | 0.8 | 0.15 | 0.19 | 1.0 |
| 3 | 1 | 0.2 | 0.2 | 1.0 |
| 4 | 1 | 0.22 | 0.22 | 1.0 |
| 5 | 0.7 | 0.15 | 0.21 | 0.8 |
| 6 | 0.6 | 0.2 | 0.33 | 1.0 |
| 7 | 0.8 | 0.2 | 0.25 | 1.0 |
| 8 | 1.0 | 0.2 | 0.2 | 1.0 |
| 9 | 1 | 0.1 | 0.1 | 1.0 |
| 10 | 1.2 | 0.2 | 0.16 | 1.1 |
| Average | 0.96 | 0.19 | 0.2 | 1.0 |

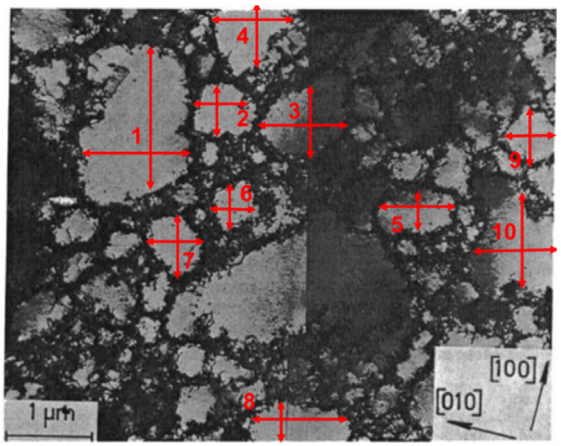


**Fig. A.17.** The TEM Cu dislocation substructure estimation strategy to estimate structure attributes for equiaxed cell structure (type III), i.e. $\eta^{III} \approx 1.0$ and $f_w^{III} \approx 0.2$. The values of cell size, aspect ratio and wall fraction measured in 10 cells and averaged.
*Source:* TEM image from Mughrabi et al. (1986).

112 Cu Crystal at 0.27 deformation, RT

| Cell No. | Dislocation structure attributes | | | |
|---|---|---|---|---|
| | D ($\mu m$) | t ($\mu m$) | $f_w = t/D$ | $\eta$ |
| 1 | 1.0 | 0.23 | 0.23 | 4.0 |
| 2 | 1.0 | 0.23 | 0.23 | 4.5 |
| 3 | 0.7 | 0.20 | 0.28 | 4.0 |
| 4 | 1.0 | 0.22 | 0.22 | 5.0 |
| 5 | 1.2 | 0.25 | 0.20 | 4.0 |
| 6 | 0.8 | 0.20 | 0.25 | 4.0 |
| 7 | 1.1 | 0.24 | 0.22 | 5.0 |
| 8 | 1.2 | 0.28 | 0.23 | 5.0 |
| 9 | 1.0 | 0.23 | 0.23 | 2.0 |
| 10 | 0.9 | 0.22 | 0.24 | 3.0 |
| Average | 0.99 | 0.23 | 0.23 | 4.0 |

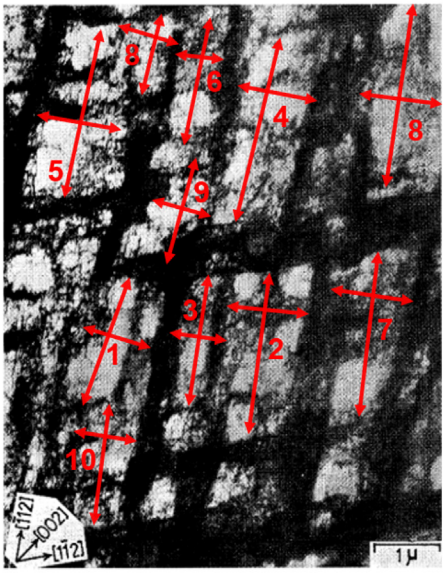


**Fig. A.18.** The TEM Cu dislocation substructure estimation strategy to estimate structure attributes for semi-elongated cell structure (type I), i.e. $\eta^{I} \approx 4.0$ and $f_w^{I} \approx 0.23$. The values of cell size, aspect ratio and wall fraction measured in 10 cells and averaged.
*Source:* TEM image from Kawasaki (1974).

dislocation activity, i.e, cross slip, Cottrell locks and Hirth locks. For each dislocation activity, a characteristic type of dislocation substructure exist: equiaxed cells for cross slip, semi-elongated cells for Cottrell locks and elongated cells for Hirth locks. The morphology of these structures can be directly quantified from TEM images. For example, $\eta$ can be approximated as the ratio between the longest and shortest space in between walls while $f_w$ can be computed as the ratio between the wall thickness and the wall spacing (Feaugas and coworkers Oudriss and Feaugas, 2016). Fig. A.17 demonstrates this methodology for equiaxed cell structures (Type III), i.e. $\eta^{III} \approx 1.0$ and $f_w^{III} \approx 0.2$. while Figs. A.18 and A.19 demonstrate the estimations of dislocation structure attributes for semi-elongated cell (Type I) and elongated cell (Type II) structures, respectively. We have repeated this measurements in 12 images for Type III, (Ambrosi et al., 1974; Kawasaki, 1979; Livingston, 1962; Huang et al., 2001; Sard and Weil, 1970; Mughrabi et al., 1986; Sumino et al., 1963), 15 images for Type I, (Kawasaki, 1974, 1979; Livingston, 1962; Sumino et al., 1963) and 9 images for Type II structures, (Sard and Weil, 1970; Sumino et al., 1963). All the measurements done at least in 10 cells per image. We note that the TEM images were selected to represent well developed structures after significant amount of straining.

110 Cu Crystal at 0.27 deformation, RT

| Cell No. | Dislocation structure attributes | | | |
|---|---|---|---|---|
| | D ($\mu m$) | t ($\mu m$) | $f_w = t/D$ | $\eta$ |
| 1 | 0.8 | 0.22 | 0.28 | 5 |
| 2 | 0.8 | 0.27 | 0.34 | 5 |
| 3 | 0.9 | 0.22 | 0.24 | 4 |
| 4 | 1 | 0.21 | 0.21 | 5 |
| 5 | 1.2 | 0.25 | 0.21 | 5 |
| 6 | 0.9 | 0.22 | 0.24 | 6 |
| 7 | 0.8 | 0.21 | 0.26 | 5 |
| Average | 1.0 | 0.23 | 0.25 | 5.0 |

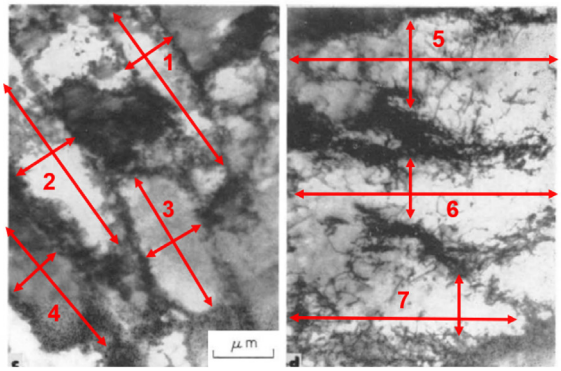


**Fig. A.19.** The TEM Cu dislocation substructure estimation strategy to estimate structure attributes for elongated cell structure (type II), i.e. $\eta^{II} \approx 5.0$ and $f_w^{II} \approx 0.25$. The values of cell size, aspect ratio and wall fraction measured in 7 cells and averaged.
*Source:* TEM image from Sard and Weil (1970).

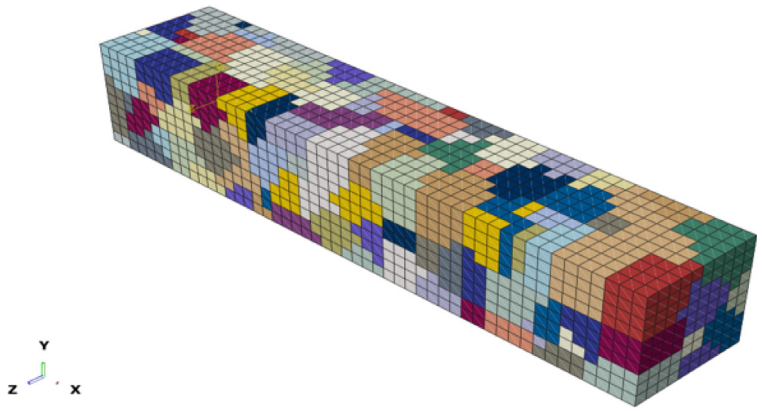


**Fig. B.20.** Finite element mesh with five thousand elements and realistic equiaxed grains. Pictorial description of different grains indicated with different colors (no correlation with Euler angles values).

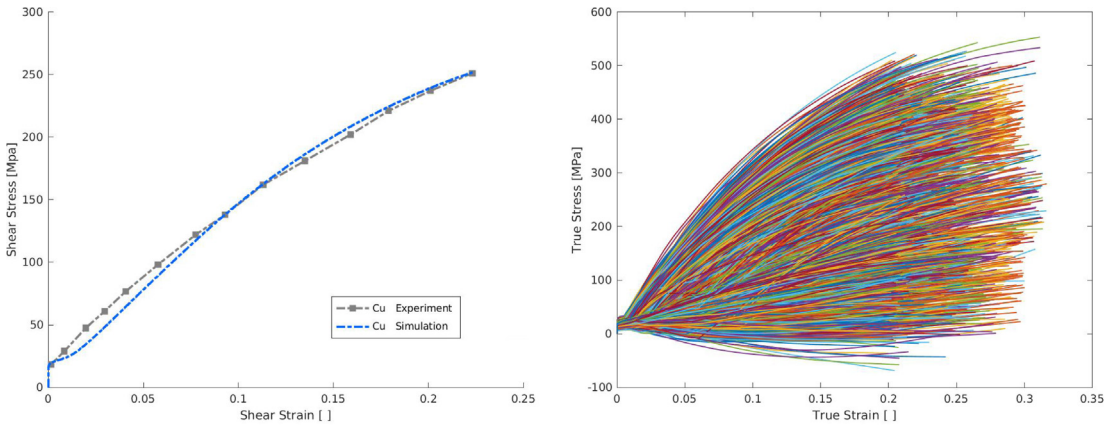


(a) (b)

**Fig. B.21.** Mechanical response of polycrystalline Cu with a realistic microstructure (a) Stress–strain response. Experimental data taken from Gracio et al. (1989). (b) Equivalent stress–strain response for five thousand elements.

## Appendix B. Effect of polycrystalline refinement

To further validate the analysis, we performed additional simulations with realistic polycrystalline microstructures as shown in Fig. B.20. The microstructure of this model was recreated using Dream3D (Groeber and Jackson, 2014) with five thousand elements

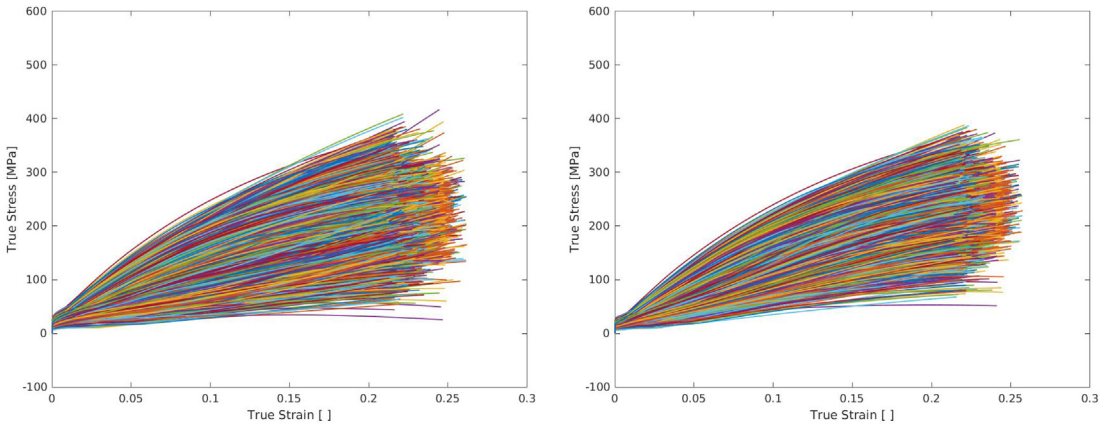


**Fig. B.22.** Grain-level equivalent stress–strain response for realistic microstructure polycrystalline Cu model using (a) $\eta = 1.4$ and (b) Eq. (25). Compared to Fig. 10, the local variability is underpredicted by isotropic mean free paths models.

and 250 equiaxed grains. Similar to prior models, straining corresponds to displacing the back face while the front face is constrained and displacements are allowed along other directions.

Fig. B.21 presents the monotonic response and the corresponding equivalent stress–strain curves for all five thousand for the realistic microstructure. These results agree with those for Cu in Figs. 9 and 10, which demonstrates the limited role of microstructure refinement on the macroscopic response, as long as enough grains are taken into consideration. We further compared equivalent stress–strain curves for all five thousand elements for the realistic microstructure using models with $\eta = 1.4$ or Eq. (25). The results in B.22 further demonstrate that these formulations reduce the intrinsic heterogeneity of slip.

## References


Alankar, A., Eisenlohr, P., Raabe, D., 2011. A dislocation density-based crystal plasticity constitutive model for prismatic slip in $\alpha$-titanium. Acta Mater. 59 (18), 7003–7009.

Ambrosi, P., Göttler, E., Schwink, C., 1974. On the dislocation arrangement and flow stress of [111] - copper single crystals deformed in tension. Scr. Metall. 8 (9), 1093–1097.

Anon, 2020. FEM software 2020, Simulia Corp., Providence, RI, USA.

Anon, 2021. Cyclic response of additive manufactured 316l stainless steel: The role of cell structures. Scr. Mater. 205, 114190.

Armstrong, R.W., Rodriguez, P., 2006. Flow stress/strain rate/grain size coupling for fcc nanopolycrystals. Phil. Mag. 86 (36), 5787–5796.

Arsenlis, A., Parks, D.M., 2002. Modeling the evolution of crystallographic dislocation density in crystal plasticity. J. Mech. Phys. Solids 50 (9), 1979–2009.

Ashraf, F., Castelluccio, G.M., 2021. A robust approach to parameterize dislocation glide energy barriers in FCC metals and alloys. J. Mater. Sci. 56 (29), 16491–16509.

Ashraf, F., Castelluccio, G.M., 2022. On the similitude relation for dislocation wall thickness under cyclic deformation. Mater. Sci. Eng. A 840, 142972. http://dx.doi.org/10.1016/j.msea.2022.142972, URL https://www.sciencedirect.com/science/article/pii/S0921509322003793.

Aslanides, A., Pontikis, V., 2000. Numerical study of the athermal annihilation of edge-dislocation dipoles. Phil. Mag. A 80 (10), 2337–2353.

Bertin, N., Capolungo, L., Beyerlein, I.J., 2013. Hybrid dislocation dynamics based strain hardening constitutive model. Int. J. Plast. 49, 119–144. http://dx.doi.org/10.1016/j.ijplas.2013.03.003, URL https://www.sciencedirect.com/science/article/pii/S0749641913000739.

Carreker, R.P., Hibbard, W.R., 1953. Tensile deformation of aluminum as a function of temperature, strain rate, and grain size. Acta Metall. 1 (6), 1157–1163.

Castelluccio, G.M., Lim, H., Emery, J.M., Battaile, C.C., 2021a. Crack tip microplasticity mediated by microstructure gradients. Fatigue Fract. Eng. Mater. Struct. 44 (9), 2337–2355.

Castelluccio, G.M., Lim, H., Emery, J.M., Battaile, C.C., 2021b. Crack tip microplasticity mediated by microstructure gradients. Fatigue Fract. Eng. Mater. Struct. 44 (9), 2337–2355. http://dx.doi.org/10.1111/ffe.13493, URL https://onlinelibrary.wiley.com/doi/abs/10.1111/ffe.13493.

Castelluccio, G.M., McDowell, D.L., 2017. Mesoscale cyclic crystal plasticity with dislocation substructures. Int. J. Plast. 98, 1–26.

Chandra, S., Samal, M.K., Chavan, V.M., Raghunathan, S., 2018. Hierarchical multiscale modeling of plasticity in copper: From single crystals to polycrystalline aggregates. Int. J. Plast. 101, 188–212.

Devincre, B., Hoc, T., Kubin, L., 2008. Dislocation mean free paths and strain hardening of crystals. Science 1688, 61–64.

El Shawish, S., Cizelj, L., 2017. Combining single- and poly-crystalline measurements for identification of crystal plasticity parameters: Application to austenitic stainless steel. Crystals 7 (6), 181.

Estrin, Y., Tóth, L.S., Molinari, A., Bréchet, Y., 1998. A dislocation-based model for all hardening stages in large strain deformation. Acta Mater. 46 (15), 5509–5522. http://dx.doi.org/10.1016/S1359-6454(98)00196-7, URL http://www.sciencedirect.com/science/article/pii/S1359645498001967.

Evans, A.G., Hutchinson, J.W., 2009. A critical assessment of theories of strain gradient plasticity. Acta Mater. 57 (5), 1675–1688. http://dx.doi.org/10.1016/j.actamat.2008.12.012, URL http://www.sciencedirect.com/science/article/pii/S1359645408008732.

Feaugas, X., 1999. On the origin of the tensile flow stress in the stainless steel AISI 316L at 300 K: back stress and effective stress. Acta Mater. 47 (13), 3617–3632.

Fivel, M., Tabourot, L., Rauch, E., Canova, G., 1998. Identification through mesoscopic simulations of macroscopic parameters of physically based constitutive equations for the plastic behaviour of fcc single crystals. Publié Dans J. Phys. 1–5.

Follansbee, P.S., Gray, G.T., 1991. The response of single crystal and polycrystal nickel to quasistatic and shock deformation. Int. J. Plast. 7 (7), 651–660.
Gracio, J.J., Fernandes, J.V., Schmitt, J.H., 1989. Effect of grain size on substructural evolution and plastic behaviour of copper. Mater. Sci. Eng. A 118 (C), 97–105.
Groeber, M.A., Jackson, M.A., 2014. DREAM.3D: A digital representation environment for the analysis of microstructure in 3D. Integr. Mater. Manuf. Innov. 3 (1), 56–72. http://dx.doi.org/10.1186/2193-9772-3-5.
Hähner, P., 1996. Stochastic dislocation patterning during cyclic plastic deformation: A theory of the formation of persistent slip band and matrix structures. Appl. Phys. A 63 (1), 45–55.
Han, F., Roters, F., Raabe, D., 2020. Microstructure-based multiscale modeling of large strain plastic deformation by coupling a full-field crystal plasticity-spectral solver with an implicit finite element solver. Int. J. Plast. 125, 97–117. http://dx.doi.org/10.1016/j.ijplas.2019.09.004, URL https://www.sciencedirect.com/science/article/pii/S0749641919303377.
Hansen, N., Huang, X., Hughes, D.A., 2001. Microstructural evolution and hardening parameters. Mater. Sci. Eng. A 317 (1–2), 3–11.
Hansen, N., Huang, X., Pantleon, W., Winther, G., 2006. Grain orientation and dislocation patterns. Phil. Mag. 86 (25–26), 3981–3994.
Hielscher, R., Schaeben, H., 2008. A novel pole figure inversion method: specification of the MTEX algorithm. J. Appl. Crystallogr. 41 (6), 1024–1037. http://dx.doi.org/10.1107/S0021889808030112.
Hirth, J.P., 1961. On dislocation interactions in the fcc lattice. J. Appl. Phys. 32 (4), 700–706.
Holt, D.L., 1970. Dislocation cell formation in metals. J. Appl. Phys. 41 (8), 3197–3201.
Huang, X., Borrego, A., Pantleon, W., 2001. Polycrystal deformation and single crystal deformation: Dislocation structure and flow stress in copper. Mater. Sci. Eng. A 319–321, 237–241.
Kakandar, E., Barrios, A., Michler, J., Maeder, X., Pierron, O.N., Castelluccio, G.M., 2020. A computational and experimental comparison on the nucleation of fatigue cracks in statistical volume elements. Int. J. Fatigue 137, 105633. http://dx.doi.org/10.1016/j.ijfatigue.2020.105633, URL http://www.sciencedirect.com/science/article/pii/S014211232030164X.
Kawasaki, Y., 1974. Cell structures in deformed copper single crystals. J. Phys. Soc. Jpn. 36 (1), 142–148.
Kawasaki, Y., 1979. Correspondence between layered cell structures and slip lines in deformed copper single crystals. Japan. J. Appl. Phys. 18 (8), 1429–1438.
Keller, C., Hug, E., 2017. Kocks-Mecking analysis of the size effects on the mechanical behavior of nickel polycrystals. Int. J. Plast. 98, 106–122. http://dx.doi.org/10.1016/j.ijplas.2017.07.003, URL http://www.sciencedirect.com/science/article/pii/S0749641917302620.
Khan, A.S., Liu, J., Yoon, J.W., Nambori, R., 2015. Strain rate effect of high purity aluminum single crystals: Experiments and simulations. Int. J. Plast. 67, 39–52.
Kocks, U.F., Argon, A.., Ashby, M.F., 1975. Thermodynamics and kinetics of slip. Prog. Mater. Sci. 19, 1–288.
Kubin, L., Sauzay, M., 2016. Persistent slip bands: Similitude and its consequences. Acta Mater. 104, 295–302.
Kuhlmann-Wilsdorf, D., Comins, N.R., 1983. Dislocation cell formation and work hardening in the unidirectional glide of f.c.c. metals I: Basic theoretical analysis of cell walls parallel to the primary glide plane in early stage II. Mater. Sci. Eng. 60 (1), 7–24.
Ledbetter, H.M., Naimon, E.R., 1974. Relationship between single-crystal and polycrystal elastic constants. J. Appl. Phys. 45 (1), 66–69.
Li, H., Jing, H., Xu, L., Han, Y., Zhao, L., Tang, Z., Xiao, B., Zhang, Y., 2019. Fatigue behavior, microstructural evolution, and fatigue life model based on dislocation annihilation of an Fe-Ni-Cr alloy at 700 C. Int. J. Plast. 118, 105–129.
Liang, D., Hure, J., Courcelle, A., Shawish, S.E., Tanguy, B., 2021. A micromechanical analysis of intergranular stress corrosion cracking of an irradiated austenitic stainless steel. Acta Mater. 204, 116482.
Lin, P., Vivekanandan, V., Castelluccio, G., Anglin, B., El-Azab, A., 2021. Crystal plasticity-inspired statistical analysis of dislocation substructures generated by continuum dislocation dynamics. Comput. Mater. Sci. In press.
Livingston, J.D., 1962. The density and distribution of dislocations in deformed copper crystals. Acta Metall. 10 (3), 229–239.
Lu, K., Chauhan, A., Tirunilai, A.S., Freudenberger, J., Kauffmann, A., Heilmaier, M., Aktaa, J., 2021. Deformation mechanisms of CoCrFeMnNi high entropy alloy under low cycle fatigue loading. Acta Mater. 215, 117089.
Lu, X., Zhang, X., Shi, M., Roters, F., Kang, G., Raabe, D., 2019. Dislocation mechanism based size-dependent crystal plasticity modeling and simulation of gradient nano-grained copper. Int. J. Plast. 113, 52–73.
McGinty, R.D., 2001. Multiscale Representation of Polycrystalline Inelasticity (Ph.D. thesis). Georgia Institute of Technology, Atlanta, GA, USA.
Mughrabi, H., Ungár, T., Kienle, W., Wilkens, M., Mughrabi, H., Ungár, T., Kienle, W., 1986. Long-range internal stresses and asymmetric X-ray line-broadening in tensile-deformed [001]-orientated copper single crystals. Philos. Mag. A 53 (6), 793–813.
Mukherjee, A.K., Mote, J.D., Dorn, J.E., 1965. Strain hardening of single aluminum crystals during polyslip. Trans. AIME 233, 1562.
Muller, M., Zehetbauer, M., Borbely, A., Ungár, T., 1996. Stage IV work hardening in cell forming materials, part I: Features of the dislocation structure determined by X-ray line broadening. Scr. Mater. 35 (12), 1461–1466. http://dx.doi.org/10.1016/S1359-6462(96)00319-3, URL http://www.sciencedirect.com/science/article/pii/S1359646296003193.
Mura, T., 1987. Micromechanics of defects in solids.pdf.
Nguyen, K., Zhang, M., Amores, V.J., Sanz, M.A., Montáns, F.J., 2021. Computational modeling of dislocation slip mechanisms in crystal plasticity: A short review. Crystals 11 (1), 1–29.
Nicolas, A., Co, N.E.C., Burns, J.T., Sangid, M.D., 2019. Predicting fatigue crack initiation from coupled microstructure and corrosion morphology effects. Eng. Fract. Mech. 220, 106661.
Oudriss, A., Feaugas, X., 2016. Length scales and scaling laws for dislocation cells developed during monotonic deformation of (001) nickel single crystal. Int. J. Plast. 78, 187–202.
Peirce, D., Asaro, R.J., Needleman, A., 1983. Material rate dependence and localized deformation in crystalline solids. Acta Metall. 31 (12), 1951–1976.
Pirgazi, H., Kestens, L.A., 2021. Semi in-situ observation of crystal rotation during cold rolling of commercially pure aluminum. Mater. Charact. 171, 110752.
Porter, E., 1992. Phase Transformations in Metals and Alloys, Vol. 66. pp. 37–39.
Rice, J., 1971. Inelastic constitutive relations for solids: An internal-variable theory and its application to metal plasticity. J. Mech. Phys. Solids 28 (9), 877.
Roters, F., Eisenlohr, P., Bieler, T.R., 2010. Crystal Plasticity Finite Element Methods.
Sard, R., Weil, R., 1970. Structure of electrodeposited copper single crystals—II. After plastic deformation. Electrochim. Acta 15 (12), 1991–1999.
Sato, M., Matsuki, Y., Hayashi, I., Kuroda, M., 2012. Yielding and strain hardening in aluminium single-crystal foils subjected to tension and bending. Phil. Mag. Lett. 92 (9), 507–516. http://dx.doi.org/10.1080/09500839.2012.691214.
Sauzay, M., Kubin, L., 2011. Scaling laws for dislocation microstructures in monotonic and cyclic deformation of fcc metals. Prog. Mater. Sci. 56 (6), 725–784.
Sedighiani, K., Diehl, M., Traka, K., Roters, F., Sietsma, J., Raabe, D., 2020. An efficient and robust approach to determine material parameters of crystal plasticity constitutive laws from macro-scale stress-strain curves. Int. J. Plast. 134, 102779.
Sedighiani, K., Traka, K., Roters, F., Raabe, D., Sietsma, J., Diehl, M., 2022. Determination and analysis of the constitutive parameters of temperature-dependent dislocation-density-based crystal plasticity models. Mech. Mater. 164, 104117.
Steeds, J., 1966. Dislocation arrangement in copper single crystals as a function of strain. Proc. R. Soc. Lond. A. 313, 509–529.
Sumino, K., Kawasaki, Y., Yamamoto, M., Sumino, M., 1963. Plastic deformation of foil copper crystals—II electron microscopical study. Acta Metall. 11 (11), 1235–1243.
Szajewski, B.A., Pavia, F., Curtin, W.A., 2015. Robust atomistic calculation of dislocation line tension. Modelling Simulation Mater. Sci. Eng. 23 (8), 85008.

Tabata, T., Fujita, H., Hiraoka, M.A., Miyake, S., 1982. The relationship between flow stress and dislocation behaviour in [111] aluminium single crystals. Philos. Mag. A 46 (5), 801–816.
Tagami, M., Kashihara, K., Okada, T., Inoko, F., 2001. Deformation structure and recrystallization in [111] aluminum single crystals deformed in tension at liquid nitrogen- and room-temperatures. Nippon Kinzoku Gakkaishi/J. Japan Inst. Met. 65 (8), 672–679.
Takeuchi, T., 1975. Work hardening of copper single crystals with multiple glide orientations. Trans. Japan Inst. Met. 16 (10), 629–640.
Thompson, A.W., 1977. Effect of grain size on work hardening in nickel. Acta Metall. 25 (1), 83–86.
Trusov, P.V., Shveykin, A.I., 2013. Multilevel crystal plasticity models of single- and polycrystals. statistical models. Phys. Mesomech. 16 (1), 23–33.
Varshni, Y.P., 1970. Temperature dependence of the elastic constants. Phys. Rev. B 2 (10), 3952–3958.
Venkatesan, P., Beshers, D., 1970. Plastic deformation in nickel crystals. Met. Trans. 1 (6), 1780–1782.
Wang, H., Capolungo, L., Clausen, B., Tomé, C.N., 2016. A crystal plasticity model based on transition state theory. Int. J. Plast. 93, 251–268.
Williamson, G.K., Smallman, R.E., 1956. III. Dislocation densities in some annealed and cold-worked metals from measurements on the X-ray debye-scherrer spectrum. Phil. Mag. 1 (1), 34–46.
Zhu, Z., Nguyen, Q., Ng, F., An, X., Liao, X., Liaw, P., Nai, S., Wei, J., 2018. Hierarchical microstructure and strengthening mechanisms of a CoCrFeNiMn high entropy alloy additively manufactured by selective laser melting. Scr. Mater. 154, 20–24.

https://dspace.org/

# Substructure-sensitive crystal plasticity with material-invariant parameters

**Dindarlou, Shahram; Castelluccio, Gustavo M.**

**2022-04-27**
Elsevier
https://doi.org/10.1016/j.ijplas.2022.103306
Dindarlou S, Castelluccio GM. (2022) Substructure-sensitive crystal plasticity with material-invariant parameters, International Journal of Plasticity, Volume 155, August 2022, Article number 103306

Downloaded from a DSpace repository. https://dspace.org/